

Towards an effective two-orbital description of Nickelate physics

Alpesh SHETH¹, Claudine LACROIX², and Sébastien BURDIN^{1*}

¹ *Université de Bordeaux, CNRS, LOMA, UMR 5798, 33400 Talence, France and*

² *Institut Néel, CNRS and Université Grenoble-Alpes,
Boite Postale 166, 38042 Grenoble Cedex 09, France*

(Dated: July 24, 2024)

Layered Nickelates have emerged as promising candidates for high-temperature superconductivity, drawing parallels to the well-studied Cuprates. This study provides a robust theoretical framework to understand the electronic structure of these materials, particularly focusing on the role of effective orbitals and the emergence of extra Fermi pocket. Using a multi-orbital model that takes into account the essential symmetries and interactions of the involved orbitals ($5d_{z^2}$, $3d_{z^2}$, $3d_{x^2-y^2}$, $2p_x$, $2p_y$, $2p_z$), we investigated the impact of the Nickel $3d_{z^2}$ orbital on the Fermi surface and the conditions that favor the emergence of a secondary Fermi surface pocket. Our findings reveal that the $3d_{z^2}$ orbital, through its exchange interactions with the rare-earth layer, can modify the Fermi surface, thus acting as a crucial element in the electronic structure. We develop an effective two-orbital model applicable to both $RNiO_3$ and $RNiO_2$ families, explaining the sensitivity of the Fermi surface to apical Oxygen presence and high-pressure environments. This model captures the evolution of the Fermi surface and predicts susceptibility features analogous to those observed in Cuprate superconductors. We observe a peak in Lindhard susceptibility in these Nickelate systems at wave vector $\mathbf{q} = (\pi, \pi)$, similar to the Cuprates. This peak can be tuned by pressure and doping.

I. INTRODUCTION

The discovery of superconductivity in hole-doped infinite-layer Nickelates such as $RNiO_2$ ($R = \text{La, Nd, Pr}$) [1–6] has sparked intensive research into their electronic structure, magnetism, and possible pairing mechanisms. One way to understand these three aspects is by comparing Nickelates to Cuprates.

Leading theories of Cuprates emphasize the CuO_2 layer as the crucial element in understanding high- T_c superconductivity [7]. Although superconductivity in Cuprates is not fully understood, modeling them becomes relatively straightforward because only one band usually crosses the Fermi level. As a result, the Hubbard model on the square lattice, which includes only Cu and O orbitals, is an applicable and widely accepted low-energy effective model for studying the Cuprate family [8].

Similar to Cuprates' $Cu^{2+} : 3d^9$ and $Cu^{3+} : 3d^8$, layered Nickelates such as $LaNiO_2$, $NdNiO_2$, and $SrNiO_2$ exhibit isoelectronic configurations of $Ni^{1+} : 3d^9$ and $Ni^{2+} : 3d^8$ [9]. Additionally, as Nickelates have a lattice structure analogous to Cuprates, it is reasonable to infer that similar to the CuO_2 layer, the NiO_2 layer plays a crucial role in developing an appropriate and effective model. However, unlike Cuprates, these layered Nickelates often have two bands that cross the Fermi level, leading to a debatable additional Fermi pocket.

Furthermore, infinite-layer Nickelates ($RNiO_2$) are nonmagnetic and weakly insulating, unlike their Cuprate analogs, which are magnetic insulators [1, 5, 10]. The absence of magnetic ordering in Nickelates intensifies the debate surrounding the superconducting mechanism

upon hole doping, particularly concerning the contrasting theories of antiferromagnetic (AFM) or ferromagnetic (FM) origin of the superconducting mechanism [11–13]. This debate is often supported by experiments exploring spin-singlet versus spin-triplet configurations in Nickelate compounds. For instance, studies comparing atomic multiplet calculations with Ni L_3 -edge X-ray absorption spectroscopy (XAS) data of $Nd_{1-x}Sr_xNiO_2$ suggest a dominance of the singlet configuration [14, 15]. Conversely, investigations involving XAS and resonant inelastic X-ray scattering (RIXS) spectra of $LaNiO_2$ indicate the prevalence of the triplet configuration [16].

Theoretically, the interaction effects in infinite-layer Nickelates ($RNiO_2$) have been extensively investigated using various approaches, such as Mott or Hund physics. [17–21]. For example, Coulomb interaction has been considered to study the emergence of superconductivity using the ab initio method such as Density Functional Theory (DFT)+U with the Wannier Downfolding methods [16, 22, 23]. In parallel, various attempts were made to explain the absence of long-range antiferromagnetism by utilizing the $t - J$ model in the strong coupling limit [24, 25]. Additionally, methods beyond DFT utilizing Dynamical Mean Field Theory (DMFT) and Dynamical Vertex Approximation were used to include Rare-earth f -orbital effects [26–28].

Perovskite Nickelates ($RNiO_3$) also have rich electronic and magnetic properties. They can exhibit phenomena such as metal-insulator transitions (MIT) charge ordering, novel magnetic phases, and bond disproportionation [29–35]. The specific mechanisms driving MIT, the electronic correlation, the nature of the electronic ground state, and the role of active orbitals and lattice distortions in $RNiO_3$ are still under active investigation [33, 34]. However, there are no reports of superconductivity in $RNiO_3$. Experimental evidence such as

* sebastien.burdin@u-bordeaux.fr

Angle-resolved Photo Emission Spectroscopy (ARPES) and ab initio calculation of $RNiO_3$ ($R = La, Nd$) suggest the predominant contribution of $3d_{x^2-y^2}$ and $3d_{z^2}$ orbitals to the Fermi surface [36, 37]. Additionally, phase boundaries and order parameters in $RNiO_3$ are robust to changes in strain, dimensionality, and heterostructure and induced changes in different order parameters [38–40].

Besides interaction effects that can generate phase transitions in Nickelates, other features concerning electronic properties have also been investigated. Experimentally, layered Nickelates ($RNiO_2$) are typically derived from the challenging topotactic reduction of the parent perovskite form of $RNiO_3$ [5]. The characteristics of the sample often depend on the synthesis process. For instance, $LaNiO_2$ synthesized using oxide molecular beam epitaxy (OBME) followed by in situ hydrogen reduction exhibits discrepancies in ARPES measurements of the Fermi-surface [41] when compared to the electronic structures predicted by *ab-initio* calculations [17, 27, 42–44]. Similarly, $NdNiO_2$ synthesized through pulse laser deposition (PLD) without any capping layer shows charge density wave (CDW) [45], while $NdNiO_2$ synthesized through OBME with a capping layer of $SrTiO_3$ shows an absence of any charge CDW [46]. Thus, density wave is sensitive to the order of Oxygen reduction and the synthesis process [47, 48]. However, the crucial role of $Ni : 3d_{x^2-y^2}$ is consistent with the reported experiments and theories for both $RNiO_3$ and $RNiO_2$. The role of other orbitals, the origin of the second Fermi-surface pocket, and density waves remain unsettled in these systems.

In this work, we will focus on the metallic paramagnetic normal states of $RNiO_3$ and $RNiO_2$. Although we recognize the significant role of interactions in the observed transitions in these systems, we will address specific questions about the contribution of orbitals from each atom to the low-energy physics. Specifically, we will examine the Fermi-surface topology, determine the particle versus hole nature of Fermi-surface pockets, and their orbital and atomic origins. Additionally, we will consider the potential emergence of density waves by static susceptibility calculation. To do this, we will examine an effective tight-binding model. Within this approach, the interaction can be viewed as either neglected or renormalized into effective tight-binding parameters of a non-interacting system.

More precisely, we present a theoretical framework for Nickelates' electronic structure, primarily focusing on the role of effective orbitals in the emergence of extra Fermi pockets. We use a multi-orbital model to examine the impact of the $3d_{z^2}$ orbital on Fermi surface topology, considering exchange interactions mediated by $3d_{z^2}$ with rare-earth layers. Our model for $RNiO_3$ and $RNiO_2$ families explains the Fermi surface's sensitivity to apical Oxygen and pressure, predicting susceptibility peaks at wave-vector $\mathbf{q} = (\pi, \pi)$. Despite the absence of direct correlation effects, significant insights can be gained from

this approach, motivating further studies to estimate and incorporate these effects using methods like the Random Phase Approximation (RPA) [49, 50].

To begin, in Section (II), we outline a generalized approach for modeling Nickelate structures, followed by detailed examinations in Sections (III A) and (III B) for both perovskite $RNiO_3$ and infinite-layered infinite-layer Nickelates ($RNiO_2$). Our unified model offers insights into how electronic structure and Fermi surface topology evolve by systematically integrating orbital degrees of freedom and their hybridization. We investigate the adjustable parameters that control the presence of additional Fermi pockets and shape the Fermi surface. We then propose an effective model that captures these characteristics while remaining computationally feasible.

Finally, in Section (V), we apply this model to static susceptibility calculations, shedding light on instabilities, enhanced response directions, and ordering tendencies.

II. GENERAL MODEL OF $RNiO_n$

This section introduces the generalized Hamiltonian formalism that encapsulates the multi-orbital nature of the $RNiO_{n=2,3}$ under consideration. We consider an equivalent 2D system with N orbitals per site of the $RNiO_{n=2,3}$, where orbitals can represent various atomic orbitals specifically belonging to R , Ni , and O . The non-interacting Hamiltonian of the system can be written in a block matrix, enabling a comprehensive description of the electronic structure within a multi-orbital framework as:

$$\mathcal{H} = \sum_i \Psi_i \tilde{\mathcal{E}}_0 \Psi_i + \sum_{\langle ij \rangle} \Psi_i \mathbf{T}_{ij} \Psi_j \quad (1)$$

where we consider a multi-orbital state using a suitable atomic basis denoted by Ψ_i^\dagger (Ψ_i), which is a row (column) matrix with elements as the creation (annihilation) operators $c_i^{\alpha\dagger}$ (c_i^α) for the orbitals α of elements R , Ni , and O at a specific site i of the compound $RNiO_n$. In $RNiO_3$, site i consists of a Rare earth and a Nickel atom with 3 Oxygen atoms, while in $RNiO_2$, site i consists of a rare earth and a Nickel atom with 2 Oxygen atoms (see Figs. 1, 2, 4, and 6). T_{ij} is a hopping matrix and $\tilde{\mathcal{E}}_0$ is an on-site energy with diagonal \mathcal{E}_0 as well as non-diagonal $\Delta\mathcal{E}_0$ elements such that $\tilde{\mathcal{E}}_0 = \mathcal{E}_0 + \Delta\mathcal{E}_0$. The elements of the diagonal part \mathcal{E}_0 are exclusively non-dispersive onsite energy $\tilde{\epsilon}_\alpha$ of orbital α of the considered $RNiO_n$. Under periodic boundary conditions, we can use the formal definition of the Fourier transformation of the basis to the momentum space as $\Psi_i^\dagger \equiv \frac{1}{\sqrt{N}} \sum_{\mathbf{k}} e^{-i\mathbf{k}\cdot\mathbf{r}_i} \Psi_{\mathbf{k}}^\dagger$ along with its adjoint. Thus, in momentum-space representation, the Hamiltonian eq. (1) can be expressed as,

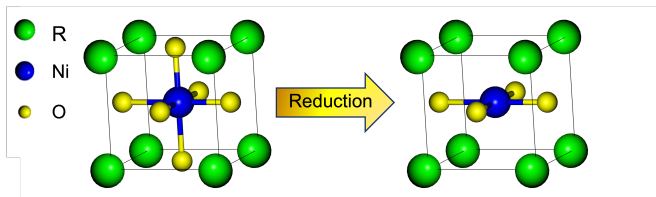


FIG. 1. Schematic crystal structures of perovskite Nickelates $RNiO_3$ (left) and layered Nickelates $RNiO_2$ (Right). The removal of apical Oxygen induces a topotactic transition from the perovskite phase to the infinite-layer phase.

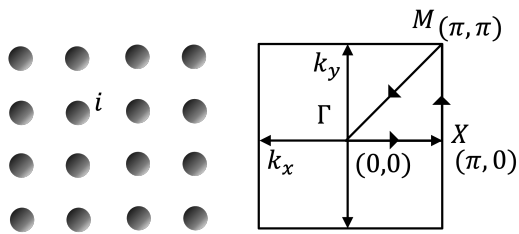


FIG. 2. Representative lattice site i and corresponding Brillouin zone. In $RNiO_3$, lattice site i consists of a Rare Earth and a Nickel atom with 3 Oxygen atoms. In $RNiO_2$, lattice site i consists of a Rare Earth and a Nickel atom with 2 Oxygen atoms.

$$\mathcal{H} = \sum_{\mathbf{k}} \Psi_{\mathbf{k}}^\dagger (\mathcal{E}_0 + \mathcal{E}_{\mathbf{k}}) \Psi_{\mathbf{k}} \quad (2a)$$

$$\mathcal{E}_{\mathbf{k}} = \Delta\mathcal{E}_0 + \sum_{\delta} \mathbf{T}_{\delta} e^{i\mathbf{k}\cdot\delta} \quad (2b)$$

thus, $\mathcal{E}_{\mathbf{k}}$ explicitly regroups the off-diagonal on-site terms $\Delta\mathcal{E}_0$ and the inter-site hopping matrix $\mathbf{T}_{\delta} e^{i\mathbf{k}\cdot\delta}$ where summation over δ accounts for the contribution over all neighbouring sites. In more convenient representation dispersion $\mathcal{E}_{\mathbf{k}}$ is,

$$\mathcal{E}_{\mathbf{k}} = \begin{bmatrix} \tilde{\varepsilon}_{\mathbf{k}}^{R-R} & \tilde{\varepsilon}_{\mathbf{k}}^{R-Ni} & \tilde{\varepsilon}_{\mathbf{k}}^{R-O} \\ \tilde{\varepsilon}_{\mathbf{k}}^{*R-Ni} & \tilde{\varepsilon}_{\mathbf{k}}^{Ni-Ni} & \tilde{\varepsilon}_{\mathbf{k}}^{Ni-O} \\ \tilde{\varepsilon}_{\mathbf{k}}^{*R-O} & \tilde{\varepsilon}_{\mathbf{k}}^{*Ni-O} & \tilde{\varepsilon}_{\mathbf{k}}^{O-O} \end{bmatrix} \quad (3)$$

where each element of dispersion $\mathcal{E}_{\mathbf{k}}^{A-B}$ is a block matrix that can take into account inter or intra-atomic energies, with $A, B \in \{R, Ni, O\}$. More specifically, these elements can be complex depending on the symmetry of the orbitals in consideration and overlap integrals of the orbitals in the crystal lattice.

Once dispersion $\mathcal{E}_{\mathbf{k}}$ is known, we can compute various electronic properties using Green's function formalism. The Green's function $\mathbb{G}_{\mathbf{k}}(\omega)$ is given by $\mathbb{G}_{\mathbf{k}}(\omega) =$

$(\omega - \mathcal{E}_0 - \mathcal{E}_{\mathbf{k}})^{-1}$, where, on general grounds, dispersion $\mathcal{E}_{\mathbf{k}}$ is given by Eq. (3) and \mathcal{E}_0 is a constant energy. We can then obtain the spectral function $\mathcal{A}_{\mathbf{k}}(\omega)$ from the imaginary part of the Green's function $\mathbb{G}_{\mathbf{k}}(\omega)$. Hence, it allows for the determination of the Fermi surface (sharp peaks at the Fermi energy) and the density of states (DoS), $\rho(\omega) = -(1/\pi)\text{ImTr}(\mathbb{G}(\omega)) = \int \text{Tr}\mathcal{A}_{\mathbf{k}}(\omega)d\mathbf{k}$ where $\mathbb{G}(\omega) = \int \mathbb{G}_{\mathbf{k}}(\omega)d\mathbf{k}$. Thus, by analyzing the spectral function, Fermi surface, and DoS obtained from the Green's function formalism for the generalized Hamiltonian defined by Eq. (3), we can gain valuable insights into the electronic structure of $RNiO_n$ system.

To ensure the broad applicability of this generalized scheme, our focus is solely on the electronic characteristics of $RNiO_n$. We have streamlined our approach by deliberately setting aside any structural complexities such as orthorhombic distortion, bond deformation, and disproportionation. This facilitates the establishment of a coherent model applicable to both $RNiO_3$ and $RNiO_2$ systems, as elaborated in Sections (III A) and (III B), respectively. Notably, in octahedral symmetry, the e_g states are always higher in energy than t_{2g} states, implying that t_{2g} states are always filled and do not play any role near the Fermi surface. The insights derived from this model pave the way for proposing an emergent effective two-orbital model for $RNiO_n$, detailed comprehensively in Section (IV).

III. EFFECTIVE MODELLING FOR $RNiO_{n=3,2}$ LAYER

A. $RNiO_3$

Recent progress in superconductivity studies in infinite-layer Nickelate ($RNiO_2$) has revealed a crucial aspect for its consistent synthesis from its parent compound in perovskite form $RNiO_3$ [5]. This study involved the production of a high-quality parent perovskite phase $RNiO_3$ (through PLD or OBME) followed by topotactic reduction to selectively eliminate apical Oxygen from the structure (as shown schematically in Fig.(1)). These layered structures, specifically $LaNiO_2$, $NdNiO_2$, $PrNiO_2$ exhibits superconductivity, when hole-doped by substituting rare-earth elements with Sr or Ca [1–6].

As mentioned previously, it is worth noting that in $RNiO_3$, the predominant contribution to the Fermi surface comes from $3d_{x^2-y^2}$ and $3d_{z^2}$ only [36]. Further, the electron hopping in $RNiO_3$ can occur through two mechanisms. The first mechanism involves two channels: the in-plane channel, where the $3d_{x^2-y^2}$ orbital hybridizes with the in-plane $2p_x$ and $2p_y$ orbitals, and the out-of-plane channel, where the $3d_{z^2}$ orbital hybridizes with the apical Oxygen $2p_z$. The second mechanism can also dominate solely through the $3d_{z^2}$ orbital hybridized with all three Oxygen atoms' $2p_x$, $2p_y$, and $2p_z$. Further, for rare-earth out-of-plane $5d_{z^2}$ is active and hybridizes with NiO plane [51].

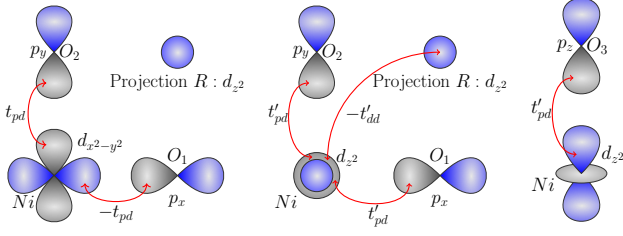


FIG. 3. Orbital overlaps and the hopping parameter considering the orbital symmetry of $RNiO_n$ and the in-plane Oxygen atoms O_1 and O_2 as well as the out-of-plane Oxygen atom O_3 .

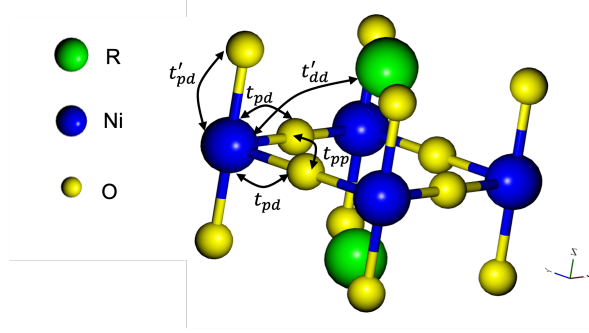


FIG. 4. Schematic of in-plane and out-plane hopping parameter in $RNiO_3$

Therefore, the generalized Hamiltonian equation (2) and the dispersion relation equation (3) incorporate the following orbitals: Rare-earth (R) atoms' - $5d_{z^2}$ orbitals, Nickel (Ni) atoms' - $3d_{x^2-y^2}$ and $3d_{z^2}$ orbitals, and Oxygen (O) atoms' $2p_{x/y/z}$ orbitals. Depending on the Oxygen atom, denoted as O_1 , O_2 , and O_3 , respectively, see in Fig (3) for each Oxygen, only one orbital amongst p_x , p_y , and p_z is important. Here, we consider hopping through neighboring Oxygen p -states as a virtual mode. Also, These equations include a block-diagonal term, representing the on-site energies of these orbitals, where the on-site energy for the $5d_{z^2}$, $3d_{z^2}$, and $3d_{x^2-y^2}$ orbitals are considered to be non-degenerate. In contrast, the on-site energies for the $2p_x$, $2p_y$, and $2p_z$ orbitals are relatively low and degenerate. As aforementioned, we are considering the low-lying Oxygen to extend the common Hamiltonian to $RNiO_2$ and $RNiO_3$ without losing its characteristic emergence phenomenon of a 2-pocket Fermi surface.

The values corresponding to the overlap of $R-O$ orbitals are set to zero in the dispersion term. This assumption is based on symmetry considerations, as illustrated in Fig. (3), which suggest no direct overlap between these

orbitals.

Thus, the blocks in eq. (3) are given by,

$$\tilde{\epsilon}_{\mathbf{k}}^{O-O} = \begin{bmatrix} 0 & t_{pp}s_{k_x}s_{k_y} & 0 \\ t_{pp}s_{k_x}^*s_{k_y} & 0 & 0 \\ 0 & 0 & 0 \end{bmatrix} \quad (4a)$$

$$\tilde{\epsilon}_{\mathbf{k}}^{Ni-O} = \begin{bmatrix} -t'_{pd}s_{k_x}^* & -t'_{pd}s_{k_y}^* & t'_{pd}s_{k_z} \\ t_{pd}s_{k_x}^* & -t_{pd}s_{k_y}^* & 0 \end{bmatrix} \quad (4b)$$

$$\tilde{\epsilon}_{\mathbf{k}}^{Ni-Ni} = \begin{bmatrix} 0 & t_{dd} \\ t_{dd} & 0 \end{bmatrix} \quad (4c)$$

$$\tilde{\epsilon}_{\mathbf{k}}^{R-R} = \tilde{\epsilon}_{5d} + t_{RR}(\cos(k_x) + \cos(k_y)) \quad (4d)$$

$$\tilde{\epsilon}_{\mathbf{k}}^{R-Ni} = \begin{bmatrix} t'_{dd}s_{k_x}s_{k_y} & t''_{dd}s_{k_x}s_{k_y} \end{bmatrix} \quad (4e)$$

where

$$s_{k_\nu} = (1 - e^{ik_\nu}) \quad (5)$$

and its complex conjugate $s_{k_\nu}^* = (1 - e^{-ik_\nu})$.

As shown in Figs. (4) and (3), the parameter labeled as t_{pd} represents the hopping parameter between $3d_{x^2-y^2} - 2p_{x/y}$ in the $x-y$ plane. t'_{pd} denotes the hopping parameter between the $3d_{z^2} - 2p_z$ out of the $x-y$ plane. The parameters t'_{dd} , t''_{dd} correspond to the hopping parameters between $5d_{z^2} - 3d_{z^2}$ and $5d_{z^2} - 3d_{x^2-y^2}$ respectively. The t_{dd} represents the hybridization between $3d_{z^2} - 3d_{x^2-y^2}$. Finally, t_{pp} denotes the hopping parameter between $2p_x - 2p_y$ in the $x-y$ plane, and t_{RR} is the hopping between the Rare-earth's $5d_{z^2}$.

The octahedral crystal field in the perovskite $RNiO_3$ compounds results in a $t_{2g} < e_g$ level splitting, where the $3d_{z^2}$ and $3d_{x^2-y^2}$ orbitals are degenerate, i.e. $\tilde{\epsilon}_{3d_{z^2}} = \tilde{\epsilon}_{3d_{x^2-y^2}}$. Crucially, our model incorporates the symmetry constraints depicted in Fig. (3), which preclude orbital overlaps between the $5d_{z^2}$ and $2p_{x/y/z}$ orbitals, as well as between the $2p_z$ and the in-plane $2p_{x/y}$ and $3d_{x^2-y^2}$ orbitals. The t'_{pd} hopping is relatively small. Furthermore, the Oxygen $2p$ levels ($\tilde{\epsilon}_{2p}$) lie well below the Fermi level $\tilde{\epsilon}_F$. Typical values for these and other relevant parameters, reported in various *ab-initio* calculations, are provided in Appendix B.

To consider the effect of apical Oxygen on orbital energies within our multi-orbital model of $RNiO_3$, as described by the dispersion eq. (4), we explore the interplay of orbitals: $5d_{z^2}$, $3d_{x^2-y^2}$, $3d_{z^2}$, and $2p_x$, $2p_y$, $2p_z$. By adjusting the relative energy scales and hopping parameters, we aim to tune our model to capture the crucial emergence of an additional Fermi pocket using a spectral function from Green's function formalism.

Our modeling approach relies on setting energy scales based on the hopping amplitude between orbitals set to

$|t_{pd}| = 1.2 \pm 0.1$, $|t_{pp}| = 0.5 \times t_{pd}$, with adjustable parameters t'_{dd} and t_{dd} . Additionally, energy scales such as,

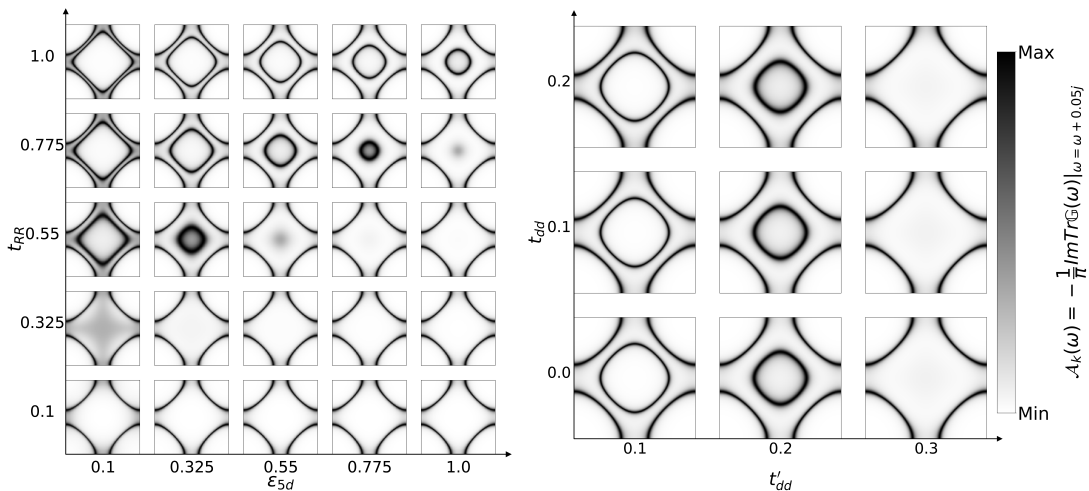


FIG. 5. Fermi surface evolution in $RNiO_3$. Left Panel: Varying t_{RR} and $\tilde{\epsilon}_{5d_{z^2}}$ for a fixed $t'_{dd} = 0.2$ and $\tilde{\epsilon}_{3d_{z^2}} = \tilde{\epsilon}_{3d_{x^2-y^2}} = -1.0$. Right panel: Varying t'_{dd} and t_{dd} for a fixed $t_{RR} = 0.775$ and $\tilde{\epsilon}_{5d_{z^2}} = 0.55$, with $\tilde{\epsilon}_{3d_{z^2}} = \tilde{\epsilon}_{3d_{x^2-y^2}} = -1.0$. Each Fermi-surface extend from $-\pi$ to π in (k_x, k_y) plane.

$\tilde{\epsilon}_{3d_{x^2-y^2}} - \tilde{\epsilon}_{5d} \approx -1.2 \times t_{pd}$, and $\tilde{\epsilon}_{3d_{x^2-y^2}} - \tilde{\epsilon}_p \approx 5 \times t_{pd}$ are established to maintain the typical order of magnitude of electronic level degeneracy and the positioning of the low-lying Oxygen level. This in general sets the $Ni : 3d$ occupancy $n_{3d_{x^2+y^2}} + n_{3d_{z^2}} \approx 3.2$ electrons as a reference. Also, since the Rare-earth has extended $5d$ -orbitals, we have explicitly considered direct $R - R$ hopping given by t_{RR} , which is tunable. This parametrization yields a Fermi surface extending from antinodal to nodal regions of the Brillouin zone, akin to the behavior observed in perovskite Nickelate. Specifically, a varying energy gap along the antinodal direction compared to the nodal direction indicates a substantially varying pocket centered at $\Gamma(0,0)$ of Fermi-surface extending from $-\pi$ to π in the high-symmetry plane of $\Gamma(0,0) - X(\pi,0) - M(\pi,\pi) - \Gamma(0,0)$, as depicted in Fig. (5).

Thus, the Fermi surface evolution depicted in Fig. (5) explores the versatility of our 6-band model's behavior, with dispersion given by eq. (4). By varying different parameters, it elucidates the interdependence of the $3d_{z^2}$ and Rare-earth $5d_{z^2}$ orbitals and the resulting formation of one or two Fermi surface pockets. As we have considered degenerate e_g near the Fermi-level, one may expect the direct contribution of these levels on the Fermi-surface. However, as aforementioned due to symmetry reasons $3d_{z^2}$ rather overlap significantly with $5d_{z^2}$ causing extended orbitals. Hopping through these extended orbitals results in the second pocket in the Fermi surface. This pocket is robust over variation of hopping amplitude between $5d_{z^2} - 3d_{z^2}$ but dormant with variation in hopping amplitude between $3d_{z^2} - 3d_{x^2-y^2}$. Thus, we can safely include the $3d_{z^2}$ as the anchoring orbital for proposing the two orbital effective model, discussed in detail in section (IV).

B. $RNiO_2$

Infinite layer Nickelate $RNiO_2$ is characterized by a square planar symmetry with alternate layers of Rare-Earth R and NiO_2 stacked along the crystallographic c -axis as depicted in Fig. (1). The square-planar coordination of Ni within NiO_2 planes and the presence of Rare-earth result in a distinctive orbital degeneracy pattern crucial in determining its electronic structure.

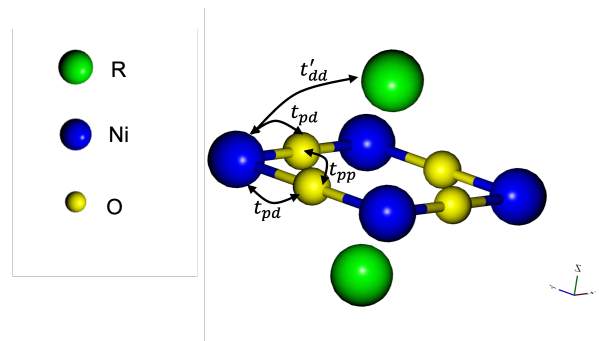


FIG. 6. Schematic of in-plane and out-plane hopping parameter in $RNiO_2$

To understand the orbital degeneracy and its effect in $RNiO_2$, we extend our model drawing analogies from the orbital symmetry description used for the related perovskite Nickelates, as depicted in Fig. (3). However, it is essential to note that in the case of $RNiO_2$, the absence of apical Oxygen ions along the z -axis leads to a different orbital ordering compared to the perovskite counterparts discussed subsequently.

The electronic structure of $RNiO_2$ is characterized by a distinctive orbital degeneracy influenced by standard square planar crystal field splitting. The transi-

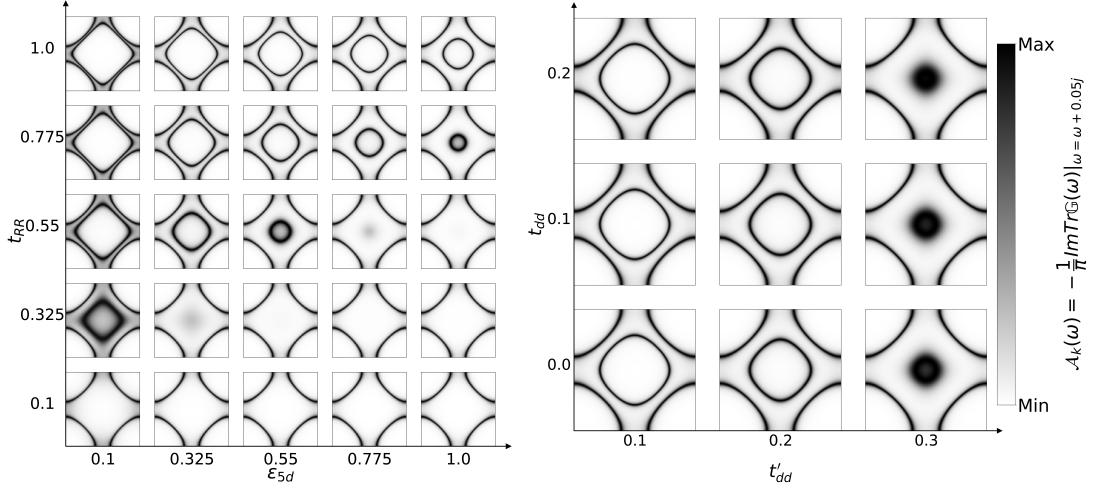


FIG. 7. Fermi surface evolution in $RNiO_2$. Left Panel: Varying t_{RR} and $\tilde{\epsilon}_{5d_{z^2}}$ for a fixed $t'_{dd} = 0.2$, $\tilde{\epsilon}_{3d_{z^2}} = -1.5$ and $\tilde{\epsilon}_{3d_{x^2-y^2}} = -1.0$. Right panel: Varying t'_{dd} and t_{dd} for a fixed $t_{RR} = 0.775$ and $\tilde{\epsilon}_{5d_{z^2}} = 0.55$, with $\tilde{\epsilon}_{3d_{z^2}} = -1.5$ and $\tilde{\epsilon}_{3d_{x^2-y^2}} = -1.0$. Each Fermi-surface extend from $-\pi$ to π in (k_x, k_y) plane.

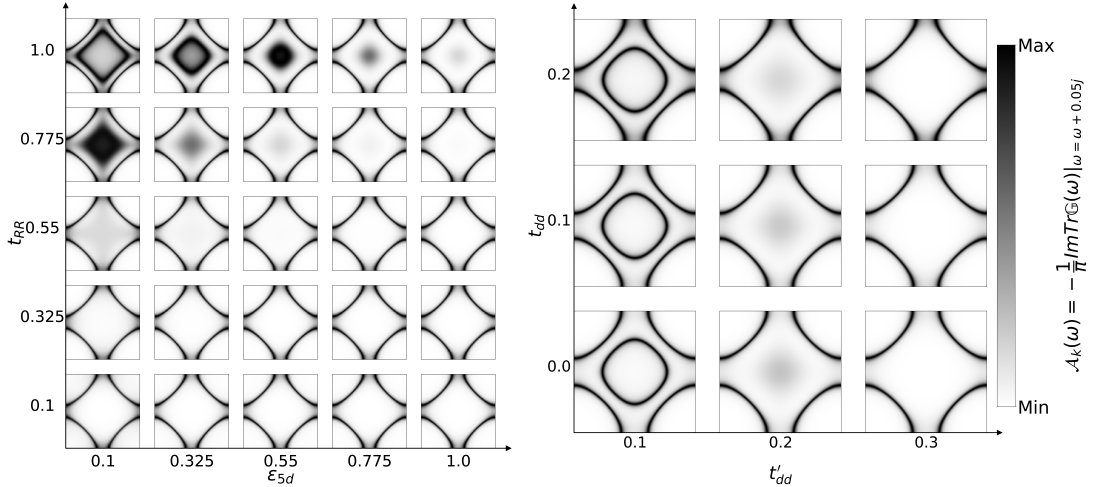


FIG. 8. Fermi surface evolution in $RNiO_2$. Left Panel: Varying t_{RR} and $\tilde{\epsilon}_{5d_{z^2}}$ for a fixed $t'_{dd} = 0.2$, $\tilde{\epsilon}_{3d_{z^2}} = -0.5$ and $\tilde{\epsilon}_{3d_{x^2-y^2}} = -1.0$. Right panel: Varying t'_{dd} and t_{dd} for a fixed $t_{RR} = 0.775$ and $\tilde{\epsilon}_{5d_{z^2}} = 0.55$, with $\tilde{\epsilon}_{3d_{z^2}} = -0.5$ and $\tilde{\epsilon}_{3d_{x^2-y^2}} = -1.0$. Each Fermi-surface extend from $-\pi$ to π in (k_x, k_y) plane.

tion from $RNiO_3$ to $RNiO_2$ involves a structural transformation from a perovskite to a square-planar arrangement through an intermediate tetragonally distorted octahedral meta-stable state. This transition resembles the stretched apical Oxygen in $RNiO_3$ and results in a degeneracy in the Ni orbitals, where $\tilde{\epsilon}_{3d_{xz}} = \tilde{\epsilon}_{3d_{yz}} < \tilde{\epsilon}_{3d_{xy}} < \tilde{\epsilon}_{3d_{z^2}} < \tilde{\epsilon}_{3d_{x^2-y^2}}$ in $RNiO_2$ [52].

Taking into account the formal valence count in $RNiO_2$, in the case of $LaNiO_2$, Lanthanum forms a La^{3+} ion, Oxygen forms an O^{2-} ion, and Nickel forms a Ni^{1+} ion. However, the general electronic configuration of Rare-Earth elements is $[Xe]4f^{(n+1)}5d^06s^2$ with exceptions for some Rare-Earth elements, where it is $[Xe]4f^n5d^16s^2$, leading to uncertainties regarding the Ni

valence state in $RNiO_2$. The non-degenerate e_g orbital in NiO_2 , together with its non-magnetic metallic nature, suggests a $d^{9-\delta}$ valence state, where $\delta = 0$ for undoped $RNiO_2$, and doping results in a transition from $3d^9$ to $3d^8$.

Further, comparisons of electron transfer in $RNiO_2$, $RNiO_3$, and Cuprates reveal differences in Mott-Hubbard-type and charge-transfer-type structures. In $RNiO_2$, while e_g splitting resembles Cuprate analogs, large $\Delta_{dp} = \tilde{\epsilon}_d - \tilde{\epsilon}_p$ exists, which determines a d^9 to d^8 transition in $RNiO_2$, contrasting with Cuprates exhibiting a d^9 to $d^9\bar{L}$ transition upon doping [22]. Notably, O K -edge XAS suggests a composite electronic state for Nickel involving both $3d^9$ and $3d^8R$ [16], where R denotes a charge-transfer to the Rare-earth cation.

The considerable Δ_{dp} in $RNiO_2$ leads to reduced $d-p$ hybridization compared to CuO_2 , supported by the orbital-resolved density of states analysis [22]. However, a RIXS measurement at the O K edge on $La_4Ni_3O_8$ indicates increased $d-p$ hybridization, alongside large Δ_{dp} and small $d-d$ Coulombic repulsion, presenting a contrast to $La_{2-x}Sr_xCuO_4$ [22].

We therefore include $5d$, $3d_{x^2-y^2}$, $3d_{z^2}$, $2p_x$ and $2p_y$ orbitals in the generalized Hamiltonian eq. (2), but exclude $2p_z$ to understand the role of planar Oxygen in these layered Nickelates. The Hamiltonian eq (2) is safely applicable, except that there is no $2p_z$ contribution. Thus, one can use eq. (4) omitting the last column and row corresponding to $2p_z$ in $\tilde{\epsilon}_{\mathbf{k}}^{Ni-O}$.

Considering the orbitals mentioned above, we can follow a similar methodology as used in the previous section (III A) to mimic the effect of reduction of apical Oxygen and compression along the z -axis. Both scenarios are associated with the emergence of superconductivity in layered Nickelates [1–6].

As previously mentioned, reducing the apical Oxygen from perovskite Nickelates results in a square planar crystal field in the $RNiO_2$ compounds. Consequently, in a $\tilde{\epsilon}_{3d_{z^2}} < \tilde{\epsilon}_{3d_{x^2-y^2}}$ level splitting, i.e. $3d_{z^2}$ and $3d_{x^2-y^2}$ orbitals are non-degenerate. While compressing along the z -axis, mimicking the Nickelates under high pressure, results in $\tilde{\epsilon}_{3d_{z^2}} > \tilde{\epsilon}_{3d_{x^2-y^2}}$ below the Fermi level. Typical values for these and other relevant parameters, reported in various *ab-initio* calculations, are provided in Appendix B.

To take into account these two effects, we again adjust the relative energy scales and hopping parameters within our 5-orbital (excluding $2p_z$ from equation (4)) as in Fig.(7) and Fig.(8) to capture the emergence of an additional Fermi-pocket using the spectral function from the Green's function formalism. This Fermi-surface evolution is subjected to setting $\tilde{\epsilon}_{3d_{z^2}} < \tilde{\epsilon}_{3d_{x^2-y^2}}$ mimicking apical Oxygen reduction and $\tilde{\epsilon}_{3d_{z^2}} > \tilde{\epsilon}_{3d_{x^2-y^2}}$ mimicking the compression along the z -axis.

This tuning helps to understand the interdependence of the $3d_{z^2}$ orbital and the rare-earth $5d$ orbital and the formation of one or two Fermi surface pockets. By comparing Figs.(5), (7), and (8), we can observe that the two-pocket Fermi-surface is more sensitive to the relative difference between $\tilde{\epsilon}_{3d_{x^2-y^2}}$ and $\tilde{\epsilon}_{3d_{z^2}}$ due to the hybridization between $5d_{z^2}$ and $3d_{z^2}$.

Because the lowered $\tilde{\epsilon}_{3d_{z^2}} < \tilde{\epsilon}_{3d_{x^2-y^2}}$ (see Fig.(7)) acts as a drain for the in-plane conducting electron and contributes as a mediator for super-exchange from $Ni-Ni$ across the layer, it is hence more robust with the change of t'_{dd} and t_{dd} while the raised $\tilde{\epsilon}_{3d_{z^2}} > \tilde{\epsilon}_{3d_{x^2-y^2}}$ (see Fig.(8)) becomes almost dormant for the emergence of an additional Fermi-pocket, which is contrary to the reason presented before. Furthermore, the condition $\tilde{\epsilon}_{3d_{z^2}} = \tilde{\epsilon}_{3d_{x^2-y^2}}$ (see Fig.(5)) shows a moderate dependence on the emergence of an additional Fermi-pocket. Hence, this analysis can infer $3d_{z^2}$ as an anchoring or-

bit level. The relative position of $3d_{z^2}$ to $3d_{x^2-y^2}$ can decide the role of $5d$ in the emergence of an additional Fermi-pocket in the Nickelates system.

IV. EFFECTIVE MODELING FOR $RNiO_n$

In the previous sections, we have shown the anchoring effect of $3d_{z^2}$, along with the impact of the presence or absence of apical Oxygen and the pressure effect on the Fermi-surface evolution. As shown in Fig. (9), we can consider, depending upon the magnitude of crystal field splitting and due to hole or electron doping, Nickel's $3d_{z^2}$ anchoring down or up Rare-earth's $5d_{z^2}$ (in terms of energy), which causes the emergence of the additional Fermi pocket.

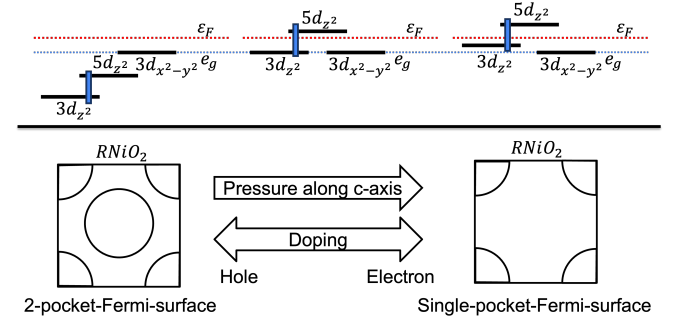


FIG. 9. Anchoring effect of Nickel: $3d_z^2$ with R: $5d_{z^2}$ and emergence of additional Fermi-surface pocket when doped with hole or electron after topotactic Reduction of an apical Oxygen from $RNiO_3$, while dormant single pocket Fermi-surface upon applying external pressure along crystallographic c -axis on $RNiO_2$.

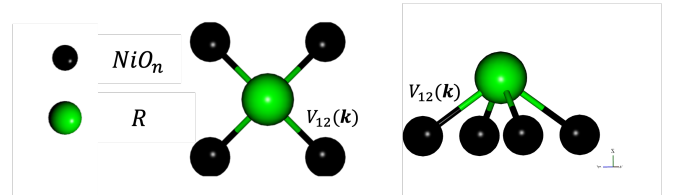


FIG. 10. Unit cell of effective $RNiO_n$ system

One may now ask, what could be an effective model that mimics those emergent features and trends of Fermi surface as discussed in detail in the previous sections (III A) and (III B) for both $RNiO_3$ and $RNiO_2$? Both $RNiO_3$ and $RNiO_2$ have approximately similar e_g bandwidth of $3eV$ [43, 53–56]. However, in $RNiO_3$, the bandwidth diminishes with confinement, coinciding with an amplified charge transfer gap Δ_{d-p} , a contracting ionic radius of R (due to Lanthanide Contraction with increasing atomic number), and an expanding lattice mismatch on which the layer is grown [53–56]. Conversely, in $RNiO_2$, the bandwidth consistently expands across

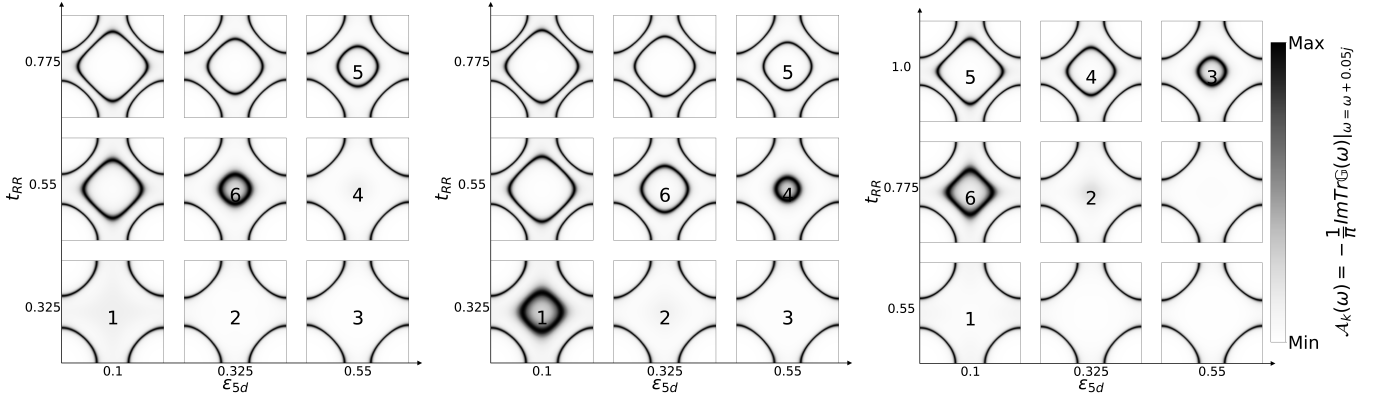


FIG. 11. Fermi surface evolution for $RNiO_n$ from our proposed effective model given by dispersion eq. (6) capturing the similar features of Fermi-surface evolution of multi-orbital model proposed in sections (III A) and (III B) for $RNiO_3$ and $RNiO_2$ respectively with condition $\tilde{\epsilon}_{3d_{z^2}} = \tilde{\epsilon}_{3d_{x^2-y^2}}$ (Left), $\tilde{\epsilon}_{3d_{z^2}} < \tilde{\epsilon}_{3d_{x^2-y^2}}$ (Middle), $\tilde{\epsilon}_{3d_{z^2}} > \tilde{\epsilon}_{3d_{x^2-y^2}}$ (Right). The number in Figures refers to the specific choice of the parameter that will be used in section V for Lindhard susceptibility calculation (see Table. I and Fig. 13).

the Lanthanide series. This phenomenon is attributed to a reduction in both in-plane [57] and out-of-plane [43] lattice constants, leading to increased orbital overlap, hybridization, and overall bandwidth.

However, an effective multi-orbital description of $RNiO_n$ along with the consideration of the presence of a second pocket Fermi Surface can be simplified considering a system consisting of two square lattices, one equivalent to the Rare-Earth layer and another equivalent NiO_n layer, with pseudo-orbital equivalent to $3d_{x^2-y^2} + 2p_{x/y}$ as shown in schematic Fig.(10). In this figure, the equivalent Rare-earth orbital-1 is in the middle of a square plaquette formed by NiO_n orbital-2, with an interlayer hybridization $V_{12}(\mathbf{k})$. Thus, we have dispersion given by,

$$\mathcal{E}_{\mathbf{k}} = \begin{bmatrix} \tilde{\mathcal{E}}_1(\mathbf{k}) & V_{12}(\mathbf{k}) \\ V_{12}^*(\mathbf{k}) & \tilde{\mathcal{E}}_2(\mathbf{k}) \end{bmatrix} \quad (6)$$

where,

$$\tilde{\mathcal{E}}_1(\mathbf{k}) = \tilde{\epsilon}_1 + 2\gamma_1(\cos(k_x) + \cos(k_y)) + 4\gamma'_1(\cos(k_x)\cos(k_y)) \quad (7)$$

corresponding to Rare-Earth,

$$\tilde{\mathcal{E}}_2(\mathbf{k}) = \tilde{\epsilon}_2 + 2\gamma_2(\cos(k_x) + \cos(k_y)) + 4\gamma'_2(\cos(k_x)\cos(k_y)) \quad (8)$$

corresponding equivalent NiO_n layer and

$$V_{12}(\mathbf{k}) = V_0 + V_1 \left(\cos\left(\frac{k_x + k_y}{2}\right) + \cos\left(\frac{k_x - k_y}{2}\right) \right) \quad (9)$$

Therefore, the proposed effective model leads to an effective two-orbital model with dispersion given by equation (6). This model is achieved through an effective

two-layer 2D square lattice system with interlayer hybridization $V_{12}(\mathbf{k})$. The key components of this approach include incorporating the effective in-plane $Ni - O - Ni$ hopping terms γ_2 and γ'_2 , which are shared by both families ($RNiO_3$ and $RNiO_2$) due to the integration of Oxygen's contribution to the effective NiO_n layer. Additionally, the formulation explicitly considers the direct $R - R$ hopping terms γ_1 and γ'_1 , which are influenced by the presence of an apical Oxygen as in $RNiO_3$. In $RNiO_3$, apical Oxygen enhances interlayer hybridization, counterbalanced by a $R - R$ direct exchange reduction.

To check the equivalence of the effective model, we down-fold the dispersion matrix eq. (3) to effective dispersion eq. (6) at a fixed set of the input parameters, which is chosen consistently according to previous sections (III A) and (III B), and calculate Fermi-surface evolution using the spectral function from the Green's function formalism as shown in Fig. (11) for all three conditions $\tilde{\epsilon}_{3d_{z^2}} = \tilde{\epsilon}_{3d_{x^2-y^2}}$, $\tilde{\epsilon}_{3d_{z^2}} < \tilde{\epsilon}_{3d_{x^2-y^2}}$, and $\tilde{\epsilon}_{3d_{z^2}} > \tilde{\epsilon}_{3d_{x^2-y^2}}$ and calculate the band-structure, density of state, and Fermi-surface at arbitrary parameters as plotted in Fig. (12). By comparison of Fig. (11) with Figs. (5), (7), and (8), we can observe that both multi-orbital model as well as effective two-orbital models have a similar emergence of two-pocket Fermi-surface.

Further, Fermi-Surface evolution, as discussed in sections (III A) and (III A), can be well understood by this effective two-band model as mentioned in eq. (6). The layer corresponds to the equivalent square lattice of NiO_n has the band-contribution from $3d_{x^2-y^2}$ and $2p_{x/y}$ orbitals. The other layer corresponds to the equivalent square lattice of $R - Ni - O$ has band-contribution from $3d_{z^2}$ and $5d_{z^2}$ orbitals, with inter-layer hybridization V_{12} , which can be momentum depended due to interstitial position of Rare-Earth.

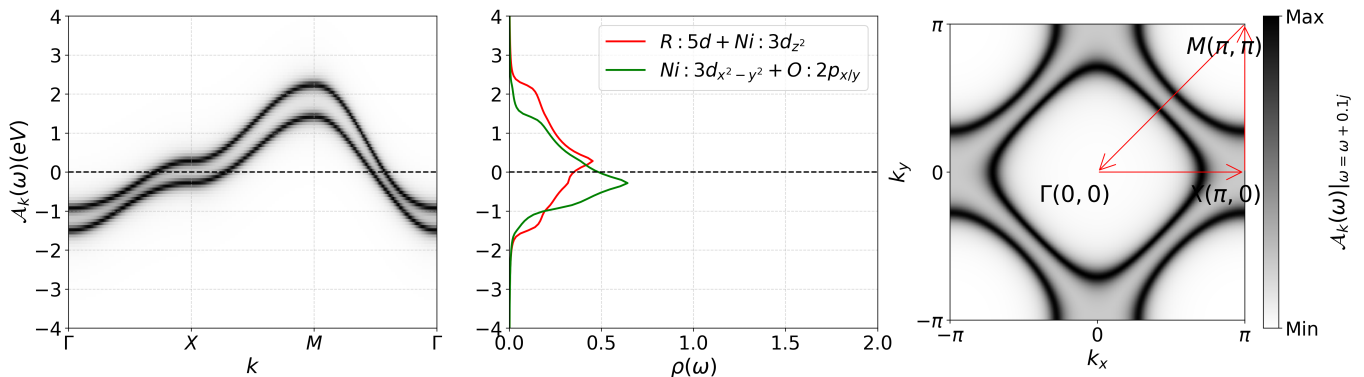


FIG. 12. **2-band Model with dispersion given by dispersion eq. (6) - Bands Structure, Orbital-Resolved Density of States and Fermi-Surface** at $\tilde{\epsilon}_{3d_{x^2-y^2}} = -1.00$, $\tilde{\epsilon}_{3d_{z^2}} = -1.70$, $t_{pp} = 0.6$, $t_{pd} = 1.2$, $\tilde{\epsilon}_{2p} = -7$, $\tilde{\epsilon}_{5d} = 0.2$, $t'_{dd} = 0.2$, $t_{dd} = 0.2$, $t_{RR} = 1.0$

Indeed, this assumption will lose the occupancy count of the band under the scrutiny of empirical evidence of input parameters and full-band Density Functional Theory (*ab-initio*) analysis. However, it will preserve a consistent trend of inter-dependence parameters and the order of magnitude and effectively gives the emergence and evolution of a two-pocket-Fermi surface.

Thus, we have developed a generalized phenomenological model based on an understanding of the relevant multi-orbital model, which consists of Nickel $3d_{z^2}$ and Rare-earth $5d_{z^2}$ in both $RNiO_3$ and $RNiO_2$ (see Fig. (9)). This has led to an effective two-orbital model for the common $RNiO_n$. Our phenomenological understanding emphasizes the role of $3d_{z^2}$ as an anchoring energy level, which in our model can be explicitly captured in the interlayer hybridization term $V_{12}(\mathbf{k})$ (see Fig. (10)) in dispersion equation (6). This effective model retains the Fermi-surface evolution features of the multi-orbital model, particularly with tuning of doping and pressure. Therefore, it can be utilized to calculate other physical observables. For example, in the subsequent section (V), we use it to calculate the static susceptibility in $RNiO_n$ systems, helping us understand the nature of electronic excitation and instabilities.

V. ANALYSIS OF LINDHARD SUSCEPTIBILITY

In undoped Cuprate parent compounds, long-range antiferromagnetic order results in distinct magnetic Bragg peaks in the susceptibility at the specific wave vector $\mathbf{q} = (\pi, \pi)$ [58–65]. However, with doping, the long-range antiferromagnetic order is quickly suppressed. Instead, the system displays short-range magnetic correlations, indicating the emergence of magnetic instabilities. This experimental behavior combined with theoret-

ical works suggests that spin fluctuations possibly have a significant contribution to the electronic pairing leading to the emergence of superconductivity [7]. In Nickelates, the dimensionality-dependent nature of spin fluctuations correlates their reduction with the appearance and subsequent disappearance of superconductivity [66, 67]. Moreover, recent findings demonstrate the pressure-dependent nature of the spin-susceptibility response in the family of bilayer 327-type Nickelates $R_3Ni_2O_7$, providing further support for the s_{\pm} -wave pairing mechanism in all candidate materials [68].

Electronic instabilities as well as charge and spin fluctuations are important for understanding the microscopic mechanism of high- T_c superconductivity. These instabilities can arise from the interplay between charge, spin, and orbital degrees of freedom, leading to transitions in the superconducting state's pairing symmetry and gap structure. In this section, we will calculate non-interacting susceptibility, also known as Lindhard susceptibility [69]. It is an important quantity that can provide insights into the ordering and excitation spectrum of materials like high- T_c Cuprate superconductors. The Lindhard susceptibility serves as the basis for calculating the fully interacting susceptibility using the Random Phase Approximation (RPA) [49, 50], which can reveal instabilities towards various ordered phases such as charge-density waves, spin-density waves, or superconductivity, depending on the dominant fluctuations within the system. We test the relevance of our effective two-orbital model eq. (6) derived from reducing a multi-orbital model eq. (4) to understand possible instabilities using Lindhard susceptibility [69].

Expressing the spin operators as $S_i^{\alpha+} = c_i^{\dagger\alpha\uparrow} c_i^{\alpha\downarrow}$ and $S_i^{\alpha-} = c_i^{\dagger\alpha\downarrow} c_i^{\alpha\uparrow}$, where α represents the orbitals corresponding to $RNiO_n$, the susceptibility as a function of imaginary time τ can be formulated as a spin-spin correlation function:

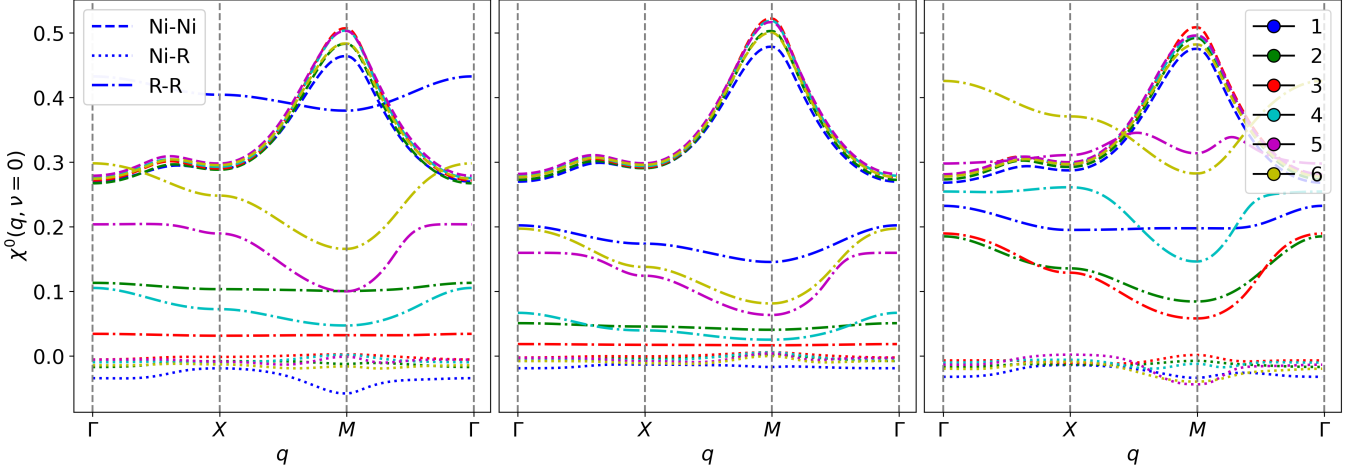


FIG. 13. Lindhard susceptibility $\chi_0(\mathbf{q}, \nu = 0)$ of $RNiO_n$ from our proposed effective model given by dispersion eq.(6) with condition $\tilde{\epsilon}_{3d_{z^2}} = \tilde{\epsilon}_{3d_{x^2-y^2}}$ (**Left**), $\tilde{\epsilon}_{3d_{z^2}} < \tilde{\epsilon}_{3d_{x^2-y^2}}$ (**Middle**), $\tilde{\epsilon}_{3d_{z^2}} > \tilde{\epsilon}_{3d_{x^2-y^2}}$ (**Right**), following path mentioned in Table (I). χ_0^{Ni-Ni} is represented by dashed lines (---), χ_0^{Ni-R} is represented by dotted lines (···) and χ_0^{R-R} is represented by the dash-dotted lines (-·-·)

$$\chi_0^{\alpha\alpha'}(\tau) = \langle S_j^{\alpha+}(\tau) S_i^{\alpha'-}(0) \rangle, \quad (10)$$

where $\langle \dots \rangle$ denotes a thermodynamic average. Here, since we neglected interaction terms in Hamiltonian the resulting susceptibility is the non-interacting one and corresponds to the Lindhard susceptibility. We find:

$$\chi_0^{\alpha\alpha'}(\tau) = -\mathcal{G}_{ij}^{\alpha\alpha'}(\tau) \mathcal{G}_{ji}^{\alpha\alpha'}(-\tau) \quad (11)$$

where $\mathcal{G}_{ij}^{\alpha\alpha'} = \langle T_\tau c_j^{\alpha\uparrow}(\tau) c_i^{\alpha'\uparrow}(0) \rangle = \langle T_\tau c_j^{\alpha\downarrow}(\tau) c_i^{\alpha'\downarrow}(0) \rangle$ represents the Green's function, and T_τ denotes the chronological order operator. Upon Fourier transformation, the static susceptibility $\chi_0(\mathbf{q}, \nu)$ is derived in reciprocal space \mathbf{k} , \mathbf{q} , and with Fermionic Matsubara frequencies $i\omega_n$:

$$\chi_0(\mathbf{q}, \nu) = -\frac{1}{\beta N} \sum_{\mathbf{k}} \sum_{\omega_n} \mathcal{G}(\mathbf{k} + \mathbf{q}, i\omega_n + \nu) \mathcal{G}(\mathbf{k}, i\omega_n) \quad (12)$$

where, ν is frequency. We dropped the element-wise representation, hence $\chi_0(\mathbf{q}, \nu = 0)$ is a matrix of static susceptibility of the system with $\chi_0^{\alpha\alpha'}$ components of orbitals in consideration. This is in principle a response of material to an external magnetic field, the peak of which also gives the optimal direction of momentum-dependent ordering.

The plots of $\chi_0(\mathbf{q}, \nu = 0)$ (Fig.(13)) for three different cases corresponding to $\tilde{\epsilon}_{3d_{z^2}} = \tilde{\epsilon}_{3d_{x^2-y^2}}$ mimicking the presence of apical Oxygen akin to perovskite Nickelates $RNiO_3$ (see left panel of Fig.(13)), $\tilde{\epsilon}_{3d_{z^2}} < \tilde{\epsilon}_{3d_{x^2-y^2}}$

mimicking the reduction of apical Oxygen akin to layered Nickelates $RNiO_2$ (see middle panel of Fig.(13)) and $\tilde{\epsilon}_{3d_{z^2}} > \tilde{\epsilon}_{3d_{x^2-y^2}}$ mimicking the layered Nickelates under high-pressure (see right panel of Fig.(13)). Each of these cases is plotted for the parameters depicted as a path in order 1 \rightarrow 6 in Fig.(11) of section (IV) from the proposed effective model given by dispersion equation (6). This path is intentionally selected to take into account all possible variations of the tunable parameter to check its effect on $\chi_0(\mathbf{q}, \nu = 0)$.

To understand the trend, consider the plotted $\chi_0(\mathbf{q}, \nu = 0)$ in Fig.13 for different paths as mentioned in Table I. When $\tilde{\epsilon}_{5d}$ varies with a constant t_{RR} , χ_0^{R-R} sequentially decreases with an increase in $\tilde{\epsilon}_{5d}$. This trend of χ_0^{R-R} is similar for all three conditions $\tilde{\epsilon}_{3d_{z^2}} = \tilde{\epsilon}_{3d_{x^2-y^2}}$, $\tilde{\epsilon}_{3d_{z^2}} < \tilde{\epsilon}_{3d_{x^2-y^2}}$, and $\tilde{\epsilon}_{3d_{z^2}} > \tilde{\epsilon}_{3d_{x^2-y^2}}$. When t_{RR} varies with a constant $\tilde{\epsilon}_{5d}$, χ_0^{R-R} sequentially increases with an increase of t_{RR} . This trend of χ_0^{R-R} is also similar for all three cases mentioned earlier. Finally, when both $\tilde{\epsilon}_{5d}$ varies with t_{RR} , χ_0^{R-R} sequentially increases with a decrease of both $\tilde{\epsilon}_{5d}$ and t_{RR} . This χ_0^{R-R} trend is consistent over all three cases. It is evident that this trend of χ_0^{R-R} becomes more dormant as the level of $\tilde{\epsilon}_{3d_{z^2}}$ as it goes further away from the Fermi level (compare the middle and right panel of Fig. (13)).

Further, χ_0^{Ni-R} is consistently near 0 throughout all the cases. χ_0^{Ni-Ni} follows the same trend as χ_0^{R-R} but is less robust compared to χ_0^{R-R} and shows a consistent peak at $\mathbf{q} = (\pi, \pi)$, which has been explicitly observed through reported *ab-initio* calculations [67, 70, 71] and a small crest at $\mathbf{q} = (\pi, 0)$ throughout all the cases. For the variation of $\tilde{\epsilon}_{5d} - t_{RR}$, χ_0^{R-R} (represented by the dotted line) shows a consistent peak at $\mathbf{q} = (0, 0)$. Also, as we

Tuning parameters		Path		
Const.	Var.	$\tilde{\epsilon}_{3d_{z^2}} = \tilde{\epsilon}_{3d_{x^2-y^2}}$ (Left)	$\tilde{\epsilon}_{3d_{z^2}} < \tilde{\epsilon}_{3d_{x^2-y^2}}$ (Middle)	$\tilde{\epsilon}_{3d_{z^2}} > \tilde{\epsilon}_{3d_{x^2-y^2}}$ (Right)
t_{RR}	$\tilde{\epsilon}_{5d}$	1 → 2 → 3	1 → 2 → 3	5 → 4 → 3
$\tilde{\epsilon}_{5d}$	t_{RR}	3 → 4 → 5	3 → 4 → 5	1 → 6 → 5
Var: $\tilde{\epsilon}_{5d}$ and t_{RR}		5 → 6	5 → 6	3 → 2 → 1

TABLE I. Table of path followed for calculating $\chi_0(\mathbf{q}, 0)$ in Fig. 13 for $RNiO_n$ from proposed effective model given by dispersion eq. 6 according to Fig. 11. For the corresponding path and condition, see Fig 11 for concern parameters.

approach the condition $\tilde{\epsilon}_{3d_{z^2}} > \tilde{\epsilon}_{3d_{x^2-y^2}}$, χ_0^{R-R} (lines in cyan and magenta color) diffused peaks near $\mathbf{q} = (\pi, 0)$ and near $\mathbf{q} = (2\pi/3, 2\pi/3)$ emerges.

Thus, we explored the Lindhard susceptibility of $RNiO_n$ with consideration of an effective two-band model derived from an equivalent multi-orbital description. This approach allows us to capture the essential physics of the system by simplifying the complex interactions into a more manageable form. Our effective model reveals a consistent susceptibility peak for the NiO_n layer at the wave vector $\mathbf{q} = (\pi, \pi)$, which is indicative of the underlying square lattice structure similar to Cuprates and potential ordering at this specific momentum transfer. Additionally, we observe a comparatively robust peak corresponding to the Rare-earth layer, highlighting the Rare-earth elements' significant role in influencing the system's electronic properties.

To understand these results, it is crucial to consider the well-established outcomes of the RPA for charge and spin susceptibilities. In the RPA framework, the susceptibility $\chi(\mathbf{q}, \nu)$ is expressed in a generalized form as $\chi(\mathbf{q}, \nu) = \chi_0(\mathbf{q}, \nu)/(1 - U_{\text{eff}}\chi_0(\mathbf{q}, \nu))$, where U_{eff} is the effective interaction strength. This formula captures how interactions renormalize the bare susceptibility, leading to enhanced responses at certain wave vectors and frequencies. Further, when the bare susceptibility $\chi_0(\mathbf{q}, \nu)$ is of the order U_{eff}^{-1} , the denominator of the RPA expression approaches zero. This condition implies that $\chi(\mathbf{q}, \nu)^{-1} \rightarrow 0$, indicating a divergence in the susceptibility [72]. Such a divergence is a hallmark of instability in the system, often leading to ordering phenomena such as charge density waves, spin density waves, or other forms of electronic ordering. This response is crucial as it contributes to the ordering behavior of the system, aligning with our observations of peaks in the susceptibility at specific wave vectors. Our model indicates that the Lindhard susceptibility peak is located at $\mathbf{q} = (\pi, \pi)$, similar to the Cuprates[58–65].

Our findings, therefore, provide a deeper understanding of the interplay between the Rare-earth elements and the NiO_n layers in determining the electronic properties and potential ordering in $RNiO_n$ compounds. In conjunction with the Lindhard susceptibility analysis with doping and pressure effects, the effective two-band model offers valuable insights into the mechanisms driving these susceptibilities and their implications for the material's

behavior. It can also reveal features like Fermi-surface nesting or van Hove singularities that significantly influence the spin fluctuation spectrum of the system. As shown in this section, this peak can be tuned either by doping or applying pressure to the system, which can aid in settling nesting features of the Fermi surface in these Nickelate systems.

VI. CONCLUSION

This study provides a comprehensive theoretical framework to understand the role of effective orbitals and the emergence of an additional Fermi pocket in layered Nickelates. By investigating the multi-orbital model of the Nickelate family and considering the appropriate symmetries of active orbitals ($5d_{z^2}, 3d_{z^2}, 3d_{x^2-y^2}, 2p_{x/y/z}$), we have identified the crucial factors that influence the electronic structure and superconductivity in these materials.

Our analysis shows that while the Nickel $3d_{x^2-y^2}$ orbital mainly crosses the Fermi level, the Nickel $3d_{z^2}$ orbital is important in lowering the energy of the Rare-earth $5d_{z^2}$ orbital. It acts as a tuning knob for the emergence of a second Fermi surface pocket. This phenomenon is particularly favored when the $3d_{z^2}$ orbital energy is lower than the $3d_{x^2-y^2}$ orbital. In this case, electrons are mediated through $5d_{z^2}$ exchange interactions between the Rare-earth and NiO_n layers.

We also developed an effective two-orbital model that captures the essential low-energy physics of the perovskite $RNiO_3$ and infinite-layer $RNiO_2$ families, considering their multi-orbital nature and intricate hybridization patterns. Our model explains the evolution of the Fermi surface topology, highlighting its sensitivity to the presence or absence of apical Oxygen and the application of high pressure. This has revealed a rich phenomenology, including the emergence of additional Fermi surface pockets and intricate susceptibility features reminiscent of those observed in Cuprate superconductors.

In particular, although we did not observe any CDW instabilities at $\mathbf{q} = (\frac{1}{3}, 0)$ (in reciprocal lattice units, r.l.u.) as suggested in some experiments [45], our findings on susceptibility indicate possible instabilities at $\mathbf{q} = (\pi, \pi)$ (or $\mathbf{q} = (\frac{1}{2}, \frac{1}{2})$ in r.l.u.), similar to those observed in Cuprates. This peak in Lindhard susceptibility could be attributed to the strong influence of the underlying

square lattice symmetry akin to Cuprates. Understanding the microscopic pairing mechanism for superconductivity, whether it involves CDW, charge order, or Magnetic Order, requires knowledge of the specific interaction terms, shedding light on the most relevant interaction and providing insights into the microscopic pairing mechanism for superconductivity. The observed Lindhard susceptibility peak at $\mathbf{q} = (\pi, \pi)$ will be crucial for the emergence of any ordering instability, including Superconductivity, that may result from microscopic interaction term. Thus, the proposed theoretical framework offers a comprehensive approach for extending models to the Nickelate family. It provides insights into the factors influencing susceptibilities, such as Fermi-surface nesting or van Hove singularities, which significantly impact the spin fluctuation spectrum.

In perspective, one could consider incorporating interactions into the proposed 2-band effective model of Nickelates, drawing inspiration from the approach used for Cuprates. This could offer valuable insights into phe-

nomena such as charge/spin Density waves, charge/spin ordering, and other instabilities that may contribute to superconductivity in the Nickelate family of materials. Expanding our theoretical predictions, we could further investigate the effects of varying doping levels and external pressures in greater detail, utilizing a combination of empirical and *ab initio*-based inputs. Additionally, conducting additional experimental studies to explore alternative potential pairing mechanisms and their implications for high-temperature superconductivity in Nickelate systems could lead to valuable insights.

ACKNOWLEDGMENTS

This work has been supported by Centre national de la recherche scientifique (CNRS) and Agence National de Recherche (ANR) grant SuperNickel (ANR-21-CE30-0041-02)

Appendix A: Susceptibility

The general form of single-particle green function in imaginary time is,

$$\mathcal{G}_{\alpha;\bar{\alpha}}(\tau_1, \tau_2) = -\langle \mathcal{T} c_{\alpha}(\tau_1) c_{\bar{\alpha}}^{\dagger}(\tau_2) \rangle \quad (\text{A1})$$

while the generalized two-particle Green's function is given by,

$$\mathcal{G}_{\bar{\alpha}\alpha;\bar{\gamma}\gamma}(\tau_1, \tau_2, \tau_3, \tau_4) = \langle \mathcal{T} c_{\bar{\alpha}}^{\dagger}(\tau_1) c_{\alpha}(\tau_2) c_{\bar{\gamma}}^{\dagger}(\tau_3) c_{\gamma}(\tau_4) \rangle \quad (\text{A2})$$

The indices $\alpha, \bar{\alpha}, \gamma, \bar{\gamma}$ can represent spin : $\{\uparrow, \downarrow\}$, orbital or band index, site index inside the unit cell, lattice site index : $i, j \in \mathcal{N}$ or momenta $\mathbf{k}, \mathbf{q} \in \mathcal{R}^3$.

For any two quadratic operator $\mathbf{A} = \sum_{ij} A_{ij} c_i^{\dagger} c_j$ and $\mathbf{B} = \sum_{ij} B_{ij} c_i^{\dagger} c_j$ most general form of the susceptibility is given by:

$$\chi_{\mathbf{A}\mathbf{B}} = \sum_{ijkl} A_{ij} \chi_{ijkl}(\omega) B_{kl} \quad (\text{A3})$$

where χ_{ijkl} is a tensor in single particle indices i, j, k, l . In imaginary time-domain $\chi_{ijkl}(\omega) \rightarrow \chi_{ijkl}(\tau)$ and it is explicitly given by following the correlation function,

$$\chi_{ijkl}(\tau_1, \tau_2, \tau_3, \tau_4) = \langle \mathcal{T} c_i^{\dagger}(\tau_1) c_j(\tau_2) c_k^{\dagger}(\tau_3) c_l(\tau_4) \rangle - \langle c_i^{\dagger}(\tau_1) c_j(\tau_2) \rangle \langle c_k^{\dagger}(\tau_3) c_l(\tau_4) \rangle \quad (\text{A4})$$

Therefore, in terms of Green's function ¹,

$$\chi_{ijkl}(\tau_1, \tau_2, \tau_3, \tau_4) = \mathcal{G}_{\bar{i}\bar{j}\bar{k}\bar{l}}(\tau_1, \tau_2, \tau_3, \tau_4) - \mathcal{G}_{ji}(\tau_2 - \tau_1) \mathcal{G}_{lk}(\tau_4 - \tau_3) \quad (\text{A5})$$

When there is no interaction, we can use Wick's Theorem, which allows us to express the two-particle Green's function by a product of single-particle Green's function with all possible pairing and with the sign given by the number of times we interchange the fermionic operator[73] and hence non-interacting susceptibility- Lindhard Susceptibility is given by,

$$\chi_{ijkl}(\tau) = \mathcal{G}_{0\ i}(-\tau) \mathcal{G}_{0\ kj}(\tau) \quad (\text{A6})$$

¹ Note the order of indices of second term

Fourier transform to Matsubara frequency $i\omega_n$ and to momentum \mathbf{k} basis

$$\chi(\mathbf{q}, \nu_n) = -\frac{1}{\beta N} \sum_{\mathbf{k}} \sum_{\omega_n} \mathcal{G}(\mathbf{k} + \mathbf{q}, i\omega_n + \nu) \mathcal{G}(\mathbf{k}, i\omega_n) \quad (\text{A7})$$

Appendix B: Parameters

Fits on <i>ab-initio</i> results:					
Compound	Ref	Orbitals	On-Site energy (eV)	NN hopping (eV)	NNN hopping (eV)
<i>LaNiO</i> ₂	[22]	<i>Ni</i> - <i>d</i> _{<i>x</i>²-<i>y</i>²}	0.249	-0.368	0.099
<i>LaNiO</i> ₂	[74]	<i>Ni</i> - <i>d</i> _{<i>x</i>²-<i>y</i>²}	0.093	-0.381	0.081
<i>LaNiO</i> ₂	[75]	<i>Ni</i> - <i>d</i> _{<i>x</i>²-<i>y</i>²}	0.281	-0.380	0.088
		Interstitial : <i>s</i>	1.493	-0.031	-0.111
<i>LaNiO</i> ₂	[76]	<i>Ni</i> - <i>d</i> _{<i>x</i>²-<i>y</i>²}	-	0.395	-0.095
<i>NdNiO</i> ₂	[77]	<i>Ni</i> - <i>d</i> _{<i>x</i>²-<i>y</i>²} + <i>O</i> - <i>p</i> _{<i>x/y</i>}	-	0.254	-0.030
<i>LaNiO</i> ₂	[26]	<i>Ni</i> - <i>d</i> _{<i>x</i>²-<i>y</i>²}	0.2689	-0.3894	0.0977
<i>NdNiO</i> ₂		<i>Ni</i> - <i>d</i> _{<i>x</i>²-<i>y</i>²}	0.2502	-0.3974	0.0933
<i>LaNiO</i> ₂	[16]	<i>Ni</i> - <i>d</i> _{<i>x</i>²-<i>y</i>²}	0.267	-0.355	-
		<i>La</i> - <i>d</i> _{<i>z</i>²}	1.132	-0.164	-

TABLE II.

Compound	Ref	Orbital	NN-hopping (eV)	NNN-hopping (eV)	$\Delta_{d_{x^2-y^2}-d_{xy}}$ (eV)
<i>LaNiO</i> ₂	[78]	<i>Ni</i> - <i>d</i> _{<i>x</i>²-<i>y</i>²}	-0.370	0.10	1.39
		<i>Ni</i> - <i>d</i> _{<i>xy</i>}	-0.16	-0.05	
<i>PrNiO</i> ₂		<i>Ni</i> - <i>d</i> _{<i>x</i>²-<i>y</i>²}	-0.370	0.10	1.41
		<i>Ni</i> - <i>d</i> _{<i>xy</i>}	-0.16	-0.05	
<i>NdNiO</i> ₂		<i>Ni</i> - <i>d</i> _{<i>x</i>²-<i>y</i>²}	-0.370	0.10	1.42
		<i>Ni</i> - <i>d</i> _{<i>xy</i>}	-0.16	-0.05	

TABLE III.

Compound	Ref.	Parameters (eV)				
<i>LaNiO</i> ₂	[22]	$\tilde{\epsilon}_p$	$\tilde{\epsilon}_{3d_{x^2-y^2}}$	$\tilde{\epsilon}_{3d_{z^2}}$	t_{pd}	t'_{pd}
		-5.41	-1.02	-1.73	-1.23	0.20
	[16]	$\tilde{\epsilon}_p$	$\tilde{\epsilon}_{3d_{x^2-y^2}}$	$\tilde{\epsilon}_{3d_{z^2}}$	t_{pd}	t'_{pd}
		-3.26	0.70	0.04	-1.20	-0.30
		$\tilde{\epsilon}_{5d_z^2}$	t'_{dd}	t''_{dd}	t_{dd}	--
		-2.42	-0.5	--	--	--
	[42]	Δ_{dp}	$\tilde{\epsilon}_{3d_{x^2-y^2}}$	$\tilde{\epsilon}_{3d_{z^2}}$	$\tilde{\epsilon}_{5d_{z^2}}$	t'_{dd}
		-6	0.40	-2.94	2.649	0.253
<i>NdNiO</i> ₂	[77]	Δ_{dp}	$\tilde{\epsilon}_{3d_{x^2-y^2}}$	t_{pd}	t_{pp}	-
		-	4.2	1.3	0.6	-

TABLE IV.

Compound	Ref	Δ_{dp} (eV)	t_{pd} (eV)
$LaNiO_3$	[79]	4.4	-1.3

TABLE V.

- [1] Shengwei Zeng, Chi Sin Tang, Xinmao Yin, Changjian Li, Mengsha Li, Zhen Huang, Junxiong Hu, Wei Liu, Ganesh Ji Omar, Hariom Jani, Zhi Shiuh Lim, Kun Han, Dongyang Wan, Ping Yang, Stephen John Pennycook, Andrew T. S. Wee, and Ariando Ariando. Phase Diagram and Superconducting Dome of Infinite-Layer $Nd_{1-x}Sr_xNiO_2$ Thin Films. *Phys. Rev. Lett.*, 125(14):147003, October 2020.
- [2] Shengwei Zeng, Changjian Li, Lin Er Chow, Yu Cao, Zhaoting Zhang, Chi Sin Tang, Xinmao Yin, Zhi Shiuh Lim, Junxiong Hu, Ping Yang, and Ariando Ariando. Superconductivity in infinite-layer nickelate $La_{1-x}Ca_xNiO_2$ thin films. *Sci. Adv.*, 8(7), February 2022.
- [3] Motoki Osada, Bai Yang Wang, Kyuho Lee, Danfeng Li, and Harold Y. Hwang. Phase diagram of infinite layer praseodymium nickelate $Pr_{1-x}Sr_xNiO_2$ thin films. *Phys. Rev. Mater.*, 4(12):121801, December 2020.
- [4] Motoki Osada, Bai Yang Wang, Berit H. Goodge, Shannon P. Harvey, Kyuho Lee, Danfeng Li, Lena F. Kourkoutis, and Harold Y. Hwang. Nickelate Superconductivity without Rare-Earth Magnetism: $(La,Sr)NiO_2$. *Adv. Mater.*, 33(45):2104083, November 2021.
- [5] Danfeng Li, Kyuho Lee, Bai Yang Wang, Motoki Osada, Samuel Crossley, Hye Ryoung Lee, Yi Cui, Yasuyuki Hikita, and Harold Y. Hwang. Superconductivity in an infinite-layer nickelate. *Nature*, 572:624–627, August 2019.
- [6] Danfeng Li, Bai Yang Wang, Kyuho Lee, Shannon P. Harvey, Motoki Osada, Berit H. Goodge, Lena F. Kourkoutis, and Harold Y. Hwang. Superconducting Dome in $Nd_{1-x}Sr_xNiO_2$ Infinite Layer Films. *Phys. Rev. Lett.*, 125(2):027001, July 2020.
- [7] Navinder Singh. Leading theories of the cuprate superconductivity: A critique. *Phys. C*, 580:1353782, January 2021.
- [8] P. W. Anderson. The Resonating Valence Bond State in La_2CuO_4 and Superconductivity. *Science*, 235(4793):1196–1198, March 1987.
- [9] V. I. Anisimov, D. Bukhvalov, and T. M. Rice. Electronic structure of possible nickelate analogs to the cuprates. *Phys. Rev. B*, 59:7901–7906, Mar 1999.
- [10] K.-W. Lee and W. E. Pickett. Infinite-layer $LaNiO_2$: Ni^{1+} is not Cu^{2+} . *Phys. Rev. B*, 70(16):165109, October 2004.
- [11] Lun-Hui Hu and Congjun Wu. Two-band model for magnetism and superconductivity in nickelates. *Phys. Rev. Res.*, 1(3):032046, December 2019.
- [12] Jennifer Fowlie, Marios Hadjimichael, Maria M. Martins, Danfeng Li, Motoki Osada, Bai Yang Wang, Kyuho Lee, Yonghun Lee, Zaher Salman, Thomas Prokscha, Jean-Marc Triscone, Harold Y. Hwang, and Andreas Suter. Intrinsic magnetism in superconducting infinite-layer nickelates. *Nat. Phys.*, 18:1043–1047, September 2022.
- [13] Ruby A. Shi, Bai Yang Wang, Yusuke Iguchi, Motoki Osada, Kyuho Lee, Berit H. Goodge, Lena F. Kourkoutis, Harold Y. Hwang, and Kathryn A. Moler. Scanning SQUID study of ferromagnetism and superconductivity in infinite-layer nickelates. *Phys. Rev. Mater.*, 8(2):024802, February 2024.
- [14] M. Rossi, H. Lu, A. Nag, D. Li, M. Osada, K. Lee, B. Y. Wang, S. Agrestini, M. Garcia-Fernandez, J. J. Kas, Y.-D. Chuang, Z. X. Shen, H. Y. Hwang, B. Moritz, Ke-Jin Zhou, T. P. Devereaux, and W. S. Lee. Orbital and spin character of doped carriers in infinite-layer nickelates. *Phys. Rev. B*, 104(22):L220505, December 2021.
- [15] Mi Jiang, Mona Berciu, and George A. Sawatzky. Critical Nature of the Ni Spin State in Doped $NdNiO_2$. *Phys. Rev. Lett.*, 124(20):207004, May 2020.
- [16] M. Hepting, D. Li, C. J. Jia, H. Lu, E. Paris, Y. Tseng, X. Feng, M. Osada, E. Been, Y. Hikita, Y.-D. Chuang, Z. Hussain, K. J. Zhou, A. Nag, M. Garcia-Fernandez, M. Rossi, H. Y. Huang, D. J. Huang, Z. X. Shen, T. Schmitt, H. Y. Hwang, B. Moritz, J. Zaanen, T. P. Devereaux, and W. S. Lee. Electronic structure of the parent compound of superconducting infinite-layer nickelates. *Nat. Mater.*, 19:381–385, April 2020.
- [17] Antia S. Botana, Kwan-Woo Lee, Michael R. Norman, Victor Pardo, and Warren E. Pickett. Low Valence Nickelates: Launching the Nickel Age of Superconductivity. *Front. Phys.*, 9:813532, February 2022.
- [18] Qiangqiang Gu and Hai-Hu Wen. Superconductivity in nickel-based 112 systems. *Innovation*, 3(1):100202, January 2022.
- [19] Yusuke Nomura and Ryotaro Arita. Superconductivity in infinite-layer nickelates. *Rep. Prog. Phys.*, 85(5):052501, March 2022.
- [20] Bai Yang Wang, Kyuho Lee, and Berit H. Goodge. Experimental Progress in Superconducting Nickelates. *Annu. Rev. Condens. Matter Phys.*, (Volume 15, 2024):305–324, March 2024.
- [21] Y. Wang, C.-J. Kang, H. Miao, and G. Kotliar. Hund’s metal physics: From $SrNiO_2$ to $LaNiO_2$. *Phys. Rev. B*, 102(16):161118, October 2020.
- [22] A. S. Botana and M. R. Norman. Similarities and differences between $LaNiO_2$ and $CaCuO_2$ and implications for superconductivity. *Phys. Rev. X*, 10:011024, Feb 2020.
- [23] Yusuke Nomura, Motoaki Hirayama, Terumasa Tadano, Yoshihide Yoshimoto, Kazuma Nakamura, and Ryotaro Arita. Formation of a two-dimensional single-component correlated electron system and band engineering in the nickelate superconductor $NdNiO_2$. *Phys. Rev. B*, 100(20):205138, November 2019.
- [24] Guang-Ming Zhang, Yi-feng Yang, and Fu-Chun Zhang. Self-doped Mott insulator for parent compounds of nickelate superconductors. *Phys. Rev. B*, 101(2):020501, January 2020.
- [25] Xianxin Wu, Domenico Di Sante, Tilman Schwemmer, Werner Hanke, Harold Y. Hwang, Srinivas Raghu, and

- Ronny Thomale. Robust $d_{x^2-y^2}$ -wave superconductivity of infinite-layer nickelates. *Phys. Rev. B*, 101(6):060504, February 2020.
- [26] Motoharu Kitatani, Liang Si, Oleg Janson, Ryotaro Arita, Zhicheng Zhong, and Karsten Held. Nickelate superconductors—a renaissance of the one-band Hubbard model. *npj Quantum Mater.*, 5(59):1–6, August 2020.
- [27] Frank Lechermann. Multiorbital Processes Rule the $\text{Nd}_{1-x}\text{Sr}_x\text{NiO}_2$ Normal State. *Phys. Rev. X*, 10(4):041002, October 2020.
- [28] Mi-Young Choi, Kwan-Woo Lee, and Warren E. Pickett. Role of $4f$ states in infinite-layer NdNiO_2 . *Phys. Rev. B*, 101:020503, Jan 2020.
- [29] M. Medarde. Structural, magnetic and electronic properties of perovskites (R = rare earth). *J. Phys.: Condens. Matter*, 1997.
- [30] C. Piamonteze, H. C. N. Tolentino, A. Y. Ramos, N. E. Massa, J. A. Alonso, M. J. Martinez-Lope, and M. T. Casais. Structural changes in RNiO_3 perovskites (R=rare earth) across the metal–insulator transition. *Physica B*, 320(1):71–74, July 2002.
- [31] J.A. Alonso, M.J. Martı́nez-Lope, J.L. Garcı́a-Muı́a \pm oz, and M.T. Fernı́ndez. Crystal structure and magnetism in the defect perovskite $\text{lanio}_{2.5}$. *Physica B: Condensed Matter*, 234-236:18–19, 1997. Proceedings of the First European Conference on Neutron Scattering.
- [32] J. L. Garcı́a-Muı́oz, J. Rodrı́guez-Carvajal, and P. Lacorre. Neutron-diffraction study of the magnetic ordering in the insulating regime of the perovskites RNiO_3 (R=Pr and Nd). *Phys. Rev. B*, 50(2):978–992, July 1994.
- [33] Valentina Bisogni, Sara Catalano, Robert J. Green, Marta Gibert, Raoul Scherwitzl, Yaobo Huang, Vladimir N. Strocov, Pavlo Zubko, Shadi Balandeh, Jean-Marc Triscone, George Sawatzky, and Thorsten Schmitt. Ground-state oxygen holes and the metal–insulator transition in the negative charge-transfer rare-earth nickelates. *Nat. Commun.*, 7(13017):1–8, October 2016.
- [34] Julien Varignon, Mathieu N. Grisolia, Jorge İñiguez, Agnès Barthélemy, and Manuel Bibes. Complete phase diagram of rare-earth nickelates from first-principles. *npj Quantum Mater.*, 2(21):1–9, April 2017.
- [35] T. Mizokawa, H. Namatame, A. Fujimori, K. Akeyama, H. Kondoh, H. Kuroda, and N. Kosugi. Origin of the band gap in the negative charge-transfer-energy compound NaCuO_2 . *Phys. Rev. Lett.*, 67(12):1638–1641, September 1991.
- [36] R. S. Dhaka, Tanmoy Das, N. C. Plumb, Z. Ristic, W. Kong, C. E. Matt, N. Xu, Kapildeb Dolui, E. Razzoli, M. Medarde, L. Patthey, M. Shi, M. Radović, and Joël Mesot. Tuning the metal-insulator transition in NdNiO_3 heterostructures via Fermi surface instability and spin fluctuations. *Phys. Rev. B*, 92(3):035127, July 2015.
- [37] P. D. C. King, H. I. Wei, Y. F. Nie, M. Uchida, C. Adamo, S. Zhu, X. He, I. Božović, D. G. Schlom, and K. M. Shen. Atomic-scale control of competing electronic phases in ultrathin LaNiO_3 . *Nat. Nanotechnol.*, 9:443–447, June 2014.
- [38] Susumu Yamamoto and Takeo Fujiwara. Charge and Spin Order in RNiO_3 (R=Nd, Y) by LSDA+U Method. *J. Phys. Soc. Jpn.*, 71(5):1226–1229, May 2002.
- [39] Jong-Woo Kim, Yongseong Choi, S. Middey, D. Meyers, J. Chakhalian, Padraic Shafer, H. Park, and Philip J. Ryan. Direct Evidence of the Competing Nature between Electronic and Lattice Breathing Order in Rare-Earth Nickelates. *Phys. Rev. Lett.*, 124(12), March 2020.
- [40] Yi Lu, Zhicheng Zhong, Maurits W. Haverkort, and Philipp Hansmann. Origins of bond and spin order in rare-earth nickelate bulk and heterostructures. *Phys. Rev. B*, 95(19):195117, May 2017.
- [41] Xiang Ding, Yu Fan, Xiaoxiao Wang, Chihao Li, Zhitong An, Jiahao Ye, Shenglin Tang, Minyanan Lei, Xingtian Sun, Nan Guo, Zhihui Chen, Suppanut Sangphet, Yilin Wang, Haichao Xu, Rui Peng, and Donglai Feng. Cuprate-like Electronic Structures in Infinite-Layer Nickelates with Substantial Hole Dopings. *Natl. Sci. Rev.*, page nwae194, June 2024.
- [42] Peiheng Jiang, Liang Si, Zhaoliang Liao, and Zhicheng Zhong. Electronic structure of rare-earth infinite-layer RNiO_2 (R = La, Nd). *Phys. Rev. B*, 100(20):201106, November 2019.
- [43] Emily Been, Wei-Sheng Lee, Harold Y. Hwang, Yi Cui, Jan Zaanen, Thomas Devereaux, Brian Moritz, and Chunjing Jia. Electronic structure trends across the rare-earth series in superconducting infinite-layer nickelates. *Phys. Rev. X*, 11:011050, Mar 2021.
- [44] Frank Lechermann. Emergent flat-band physics in $d^{9-\delta}$ multilayer nickelates. *Phys. Rev. B*, 105(15):155109, April 2022.
- [45] Charles C. Tam, Jaewon Choi, Xiang Ding, Stefano Agrestini, Abhishek Nag, Mei Wu, Bing Huang, Huiqian Luo, Peng Gao, Mirian Garcı́a-Fernández, Liang Qiao, and Ke-Jin Zhou. Charge density waves in infinite-layer NdNiO_2 nickelates. *Nat. Mater.*, 21:1116–1120, October 2022.
- [46] C. T. Parzyck, N. K. Gupta, Y. Wu, V. Anil, L. Bhatt, M. Bouliane, R. Gong, B. Z. Gregory, A. Luo, R. Sartaro, F. He, Y.-D. Chuang, T. Zhou, G. Herranz, L. F. Kourkoutis, A. Singer, D. G. Schlom, D. G. Hawthorn, and K. M. Shen. Absence of $3a_0$ charge density wave order in the infinite-layer nickelate NdNiO_2 . *Nat. Mater.*, 23:486–491, April 2024.
- [47] G. Krieger, L. Martinelli, S. Zeng, L. E. Chow, K. Kummer, R. Arpaia, M. Moretti Sala, N. B. Brookes, A. Ariando, N. Viart, M. Salluzzo, G. Ghiringhelli, and D. Preziosi. Charge and Spin Order Dichotomy in NdNiO_2 Driven by the Capping Layer. *Phys. Rev. Lett.*, 129(2):027002, July 2022.
- [48] Xiaolin Ren, Ronny Sutarto, Qiang Gao, Qisi Wang, Jiarui Li, Yao Wang, Tao Xiang, Jiangping Hu, J. Chang, Riccardo Comin, X. J. Zhou, and Zhihai Zhu. Two Distinct Charge Orders in Infinite-layer $\text{PrNiO}_2+\{\delta\}$ revealed by Resonant X-ray Diffraction. *arXiv*, March 2023.
- [49] P. W. Anderson. Random-Phase Approximation in the Theory of Superconductivity. *Phys. Rev.*, 112(6):1900–1916, December 1958.
- [50] Giampaolo Co’. Introducing the random phase approximation theory. *Universe*, 9(3):141, 2023.
- [51] Mingjing Chen, Xingkun Ning, Guangsheng Fu, Shuang Guo, Lingyun Wang, Peng Liu, Jianglong Wang, Shufang Wang, Wei Liu, Jirong Sun, et al. The role of pd hybridization in the metal-insulator transition in NdNiO_3 heterostructure. *Mater. Res. Lett.*, September 2018.
- [52] JJ Zuckerman. Crystal field splitting diagrams. *Journal of Chemical Education*, 42(6):315, 1965.
- [53] Alexandru B. Georgescu, Oleg E. Peil, Ankit S. Disa, An-

- toine Georges, and Andrew J. Millis. Disentangling lattice and electronic contributions to the metal–insulator transition from bulk vs. layer confined RNiO₃. *Proc. Natl. Acad. Sci. U.S.A.*, 116(29):14434–14439, July 2019.
- [54] Andreas Rüegg, Chandrima Mitra, Alexander A. Demkov, and Gregory A. Fiete. Electronic structure of (LaNiO₃)₂/(LaAlO₃)_N heterostructures grown along [111]. *Phys. Rev. B*, 85:245131, Jun 2012.
- [55] Jian Liu, Mehdi Kargarian, Mikhail Kareev, Ben Gray, Phil J. Ryan, Alejandro Cruz, Nadeem Tahir, Yi-De Chuang, Jinghua Guo, James M. Rondinelli, et al. Heterointerface engineered electronic and magnetic phases of NdNiO₃ thin films. *Nat. Commun.*, 4(2714):1–11, November 2013.
- [56] J.-S. Zhou, J. B. Goodenough, and B. Dabrowski. Exchange Interaction in the Insulating Phase of RNiO₃. *Phys. Rev. Lett.*, 95:127204, Sep 2005.
- [57] Electronic structure and magnetism in infinite-layer nickelates RNiO₂ ($R = \text{La}–\text{Lu}$), author = Kapeghian, Jesse and Botana, Antia S. *Phys. Rev. B*, 102:205130, Nov 2020.
- [58] A. A. Vladimirov, D. Ihle, and N. M. Plakida. Dynamic spin susceptibility of superconducting cuprates: A microscopic theory of the magnetic resonance mode. *Phys. Rev. B*, 83(2):024411, January 2011.
- [59] Y. Sidis, S. Pailhès, B. Keimer, P. Bourges, C. Ulrich, and L. P. Regnault. Magnetic resonant excitations in High-T_c superconductors. *Phys. Status Solidi B*, 241(6):1204–1210, May 2004.
- [60] Yvan Sidis, Stéphane Pailhès, Vladimir Hinkov, Benoît Fauqué, Clemens Ulrich, Lucia Capogna, Alexandre Ivanov, Louis-Pierre Regnault, Bernhard Keimer, and Philippe Bourges. Inelastic neutron scattering study of spin excitations in the superconducting state of high temperature superconductors. *C. R. Phys.*, 8(7-8):745–762, 2007.
- [61] Matthias Eschrig. The effect of collective spin-1 excitations on electronic spectra in high- T_c superconductors. *Adv. Phys.*, January 2006.
- [62] Qimiao Si, Yuyao Zha, K. Levin, and J. P. Lu. Comparison of spin dynamics in YBa₂Cu₃O_{7- δ} and La_{2- x} Sr _{x} CuO₄: Effects of Fermi-surface geometry. *Phys. Rev. B*, 47(14):9055–9076, April 1993.
- [63] H. F. Fong, P. Bourges, Y. Sidis, L. P. Regnault, J. Bossy, A. Ivanov, D. L. Milius, I. A. Aksay, and B. Keimer. Spin susceptibility in underdoped YBa₂Cu₃O_{6+ x} . *Phys. Rev. B*, 61(21):14773–14786, June 2000.
- [64] Pengcheng Dai, H. A. Mook, R. D. Hunt, and F. Doğan. Evolution of the resonance and incommensurate spin fluctuations in superconducting YBa₂Cu₃O_{6+ x} . *Phys. Rev. B*, 63(5):054525, January 2001.
- [65] Hiroyuki Yamase and Walter Metzner. Magnetic excitations and their anisotropy in YBa₂Cu₃O_{6+ x} : Slave-boson mean-field analysis of the bilayer t - J model. *Phys. Rev. B*, 73(21):214517, June 2006.
- [66] Christopher Lane, Ruiqi Zhang, Bernardo Barbiellini, Robert S. Markiewicz, Arun Bansil, Jianwei Sun, and Jian-Xin Zhu. Competing incommensurate spin fluctuations and magnetic excitations in infinite-layer nickelate superconductors. *Commun. Phys.*, 6(90):1–11, May 2023.
- [67] Fangze Liu, Cheng Peng, Edwin W. Huang, Brian Moritz, Chunjing Jia, and Thomas P. Devereaux. Emergence of antiferromagnetic correlations and Kondolike features in a model for infinite layer nickelates. *npj Quantum Mater.*, 9(49):1–7, June 2024.
- [68] Yang Zhang, Ling-Fang Lin, Adriana Moreo, Thomas A. Maier, and Elbio Dagotto. Trends in electronic structures and s_{\pm} -wave pairing for the rare-earth series in bilayer nickelate superconductor R₃Ni₂O₇. *Phys. Rev. B*, 108(16):165141, October 2023.
- [69] Henrik Smith. The Lindhard Function and the Teaching of Solid State Physics. *Phys. Scr.*, 28(3):287, September 1983.
- [70] Chao Chen, Runyu Ma, XueLei Sui, Ying Liang, Bing Huang, and Tianxing Ma. Antiferromagnetic fluctuations and dominant d_{xy} -wave pairing symmetry in nickelate-based superconductors. *Phys. Rev. B*, 106(19):195112, November 2022.
- [71] Tao Zhou, Yi Gao, and ZiDan Wang. Spin excitations in nickelate superconductors. *Sci. China Phys. Mech. Astron.*, 63(8):1–9, August 2020.
- [72] Bharathiganesh Devanarayanan, Akariti Sharma, Alpesh Sheth, Prafulla K. Jha, and Navinder Singh. Background for the Self Consistent Renormalisation (SCR) Theory. *arXiv*, August 2021.
- [73] Henrik Bruus and Karsten Flensberg. *Many-body quantum theory in condensed matter physics: an introduction*. OUP Oxford, 2004.
- [74] K.-W. Lee and W. E. Pickett. Infinite-layer LaNiO₂: Ni¹⁺ is not Cu²⁺. *Phys. Rev. B*, 70:165109, Oct 2004.
- [75] Tharathep Plienbumrung, Maria Daghofer, Michael Schmid, and Andrzej M. Oleś. Screening in a two-band model for superconducting infinite-layer nickelate. *Phys. Rev. B*, 106(13):134504, October 2022.
- [76] Marcel Klett, Philipp Hansmann, and Thomas Schäfer. Magnetic Properties and Pseudogap Formation in Infinite-Layer Nickelates: Insights From the Single-Band Hubbard Model. *Front. Phys.*, 10:834682, February 2022.
- [77] Hu Zhang, Lipeng Jin, Shanmin Wang, Bin Xi, Xingqiang Shi, Fei Ye, and Jia-Wei Mei. Effective Hamiltonian for nickelate oxides Nd_{1- x} Sr _{x} NiO₂. *Phys. Rev. Res.*, 2(1):013214, February 2020.
- [78] T. Y. Xie, Z. Liu, Chao Cao, Z. F. Wang, J. L. Yang, and W. Zhu. Microscopic theory of superconducting phase diagram in infinite-layer nickelates. *Phys. Rev. B*, 106(3):035111, July 2022.
- [79] Alejandro Lopez-Bezanilla, Louis-François Arsenault, Anand Bhattacharya, Peter B. Littlewood, and Andrew J. Millis. Parameter transferability, self-doping, and metallicity in LaNiO₃/LaMnO₃ superlattices. *Phys. Rev. B*, 99(3):035133, January 2019.